EFFECT OF NOZZLE GEOMETRY ON THE EFFICIENCY OF COMPRESSED AIR NOZZLES

Slootmaekers T.*, Slaets P., Bartsoen T.**, Malfait L.** and Vanierschot M.

*Author for correspondence
University of Leuven,
Faculty of Engineering Technology,
Campus Group T Leuven,
Andreas Vesaliusstraat 13,
3000 Leuven, Belgium,
E-mail: tim.slootmaekers@kuleuven.be

**Katholieke Hogeschool VIVES – Associatie KU Leuven,
Doorniksesteenweg 145,
8500 Kortrijk, Belgium

ABSTRACT

This paper evaluates the performance of different nozzle geometries which are all used in industrial blowing applications. Five different geometries were selected: a converging nozzle, a stepped nozzle, a straight pipe, a converging-diverging nozzle and an energy-efficient nozzle. The flow field of the various nozzles was calculated using CFD simulations. The compressible RANS equations were solved using the SST k-omega turbulence model. Different properties, like the total impact force, the impact pressure and the entrainment rate were obtained from the simulations to compare the nozzles with each other. For each of these properties, the most efficient nozzle was the one for which the mass flow rate of compressed air was the lowest. All nozzles showed comparable mass flow rates for the same impact force and the difference was in the order of 5% better than a straight pipe geometry. Only the energy saving nozzle used around 10% less mass flow and is the best solution to reduce compressed air consumption without losing performance.

INTRODUCTION

Compressed air is a common energy medium. In Europe 10% of all industrial electric energy consumption is used to make compressed-air, which is equivalent to 80 TWh each year [1]. However, compressed air acts as a hidden cost in many companies. The production of compressed air itself is not a very efficient process. Avoiding any unnecessary losses of air can lead to large reductions in electricity consumption. There has already been some initiative to quantify the energy losses in Europe [2] [3] and the USA [4]. It is important that companies understand the huge cost of using compressed-air. Since blowing applications are one of the main domains were compressed-air is used [5], any reduction in the mass flow needed for operation can lead to significant energy savings. There has already been research on the general behaviour of jets with the focus on the use as rocket propulsion [6], [7]. The geometry of the converging-diverging jets was adjusted to maximize the thrust. Also numerical simulations were used to maximise this thrust and evaluation of different turbulence models showed that the k-ω SST model in combination with the density based solver gives the best results for predicting the flow field of supersonic jets [8].

Since most of the studies on nozzles are focussing on jet propulsion, we try to fill a gap in the literature by putting our focus on nozzles for industrial use in a compressed air system. Five geometries were selected, a converging nozzle (Figure 2), a stepped nozzle (Figure 1), a straight pipe, a converging-diverging nozzle (Figure 3) and an energy-efficient nozzle (Figure 4). The energy efficient nozzle is a combination of a stepped nozzle and a diverging part connected at the back. This geometry permits the surrounding air to be entrained.

NOMENCLATURE

D	[m]	Outlet diameter nozzle
x	[m]	Axial distance measured from outlet nozzle
r	[m]	Radial distance measured from centreline nozzle
V	[m/s]	Velocity of the air
ρ	[kg/m³]	Density of the air
$\dot{m}$	[kg/s]	Mass flow rate
F	[N]	Force generated by the nozzle
f_s	[N/(Nm³/h)]	Specific force generated by the nozzle. This is F divided by Q_N
p	[Pa]	Static pressure
Q	[m³/s]	Volumetric flow rate
Q_N	[Nm³/h]	Volumetric flow rate at normal conditions
R	[J/(kgK)]	Gas constant
φ	[-]	Entrainment rate

Subscripts		
g		Gauge
$surr$		Surroundings
N		Normal conditions
out		Outlet nozzle
in		Inlet nozzle
x		Vector component in axial direction
r		Vector component in radial direction

All nozzles have been simulated with the same outlet diameter and nozzle length at 5 bar$_g$ inlet pressure. A grid study was performed to ensure that the CFD results were sufficiently grid independent. Various properties of the jet were calculated from the simulations, such as the impact force and volumetric

flow rate at normal conditions. Comparison of these properties allows comparing of the performance of these different nozzles with each other.
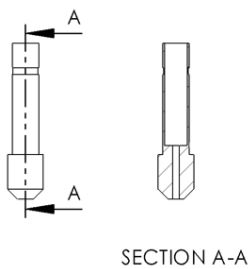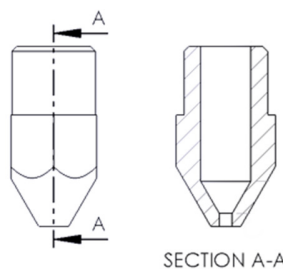

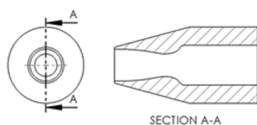**Figure 1** Stepped nozzle   **Figure 2** Converging nozzle
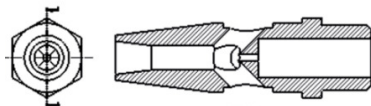

Figure 3 Converging-diverging nozzle

Figure 4 Energy saving nozzle

NUMERICAL METHODS AND BOUNDARY CONDITIONS

Since the nozzles are axisymmetric, a 2D computational domain was chosen. The axisymmetric variant of the equations of motion in cylindrical coordinates in a (xr)-plane are solved. Figure 5 shows the computational domain and boundary conditions. More details can be found in Table 1. The 2D axisymmetric RANS equations were solved using a density based solver. This solver is very robust for capturing shockwaves [8]. As a turbulence model, the k-ω SST model was chosen. This model is considered in literature to be the best model for simulating compressible jet flows [8], [9]. As a working fluid air is chosen which is treated as an ideal gas.
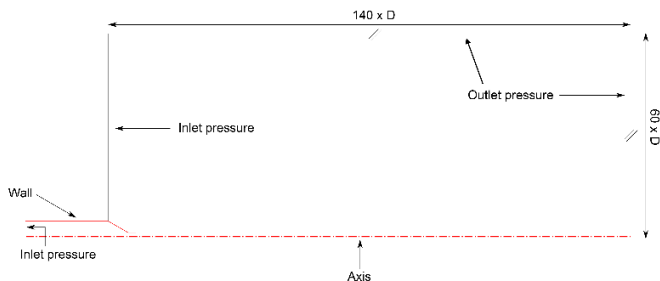

Figure 5 Computational domain and boundary conditions

A structured 2D mesh was used which is locally refined during the calculations. These refining steps are necessary to correctly capture the shock waves without needing an excessive amount of extra grid cells. A grid study was performed to ensure that the results are sufficiently grid independent and Table 2 shows the sizes of the different meshes used.

Table 1 Boundary conditions

	Boundary condition	Input values
Inlet nozzle	Inlet pressure	5 bar$_g$
Inlet surroundings	Inlet pressure	0 bar$_g$
Top surroundings	Outlet pressure	0 bar$_g$
Nozzle	Wall	Adiabatic
Axis	Axis	

Table 2 Grid study

|	
Coarse mesh	60.000 cells
Middle mesh	100.000 cells
Fine mesh	185.000 cells

The difference in velocity fields between the fine and coarse mesh is less than 0.5%. The mass flow rate and impact force at the outlet of the nozzle are calculated as well for the three meshes. Table 3 shows the results for the jet mass flow. The differences between the coarse and fine meshes are within 0.4%. With respect to the impact force, the difference between the coarse and middle mesh is smaller than 1.4% and the difference between the fine and the middle mesh is below 0.5%. These results show that solution of the middle mesh is already sufficient grid independent and to not lengthen the computations too much, this mesh was preferred over the fine one of 185.000 cells.

Table 3 Comparison of grid study results for mass flow rate

	Mass flow (x 10^{-3} kg/s)	Percent deviation from middle mesh (%)
Middle mesh	1.7350	
Coarse mesh	1.7296	0.30
Fine mesh	1.7356	0.03

RESULTS AND DISCUSSION

The numerical setup, turbulence model and boundary conditions used were validated using the experimental data published by Eggers [10]. Comparison of the results shows that the numerical calculations can capture the shocks quite accurate and predict the velocity profiles in the radial direction and the decay of centerline velocity very well for downstream directions up to x/D = 15 (Figure 6, Figure 7). Further downstream, the velocity decay is slightly over predicted as the turbulence model has a higher momentum decay than the experimental jet.
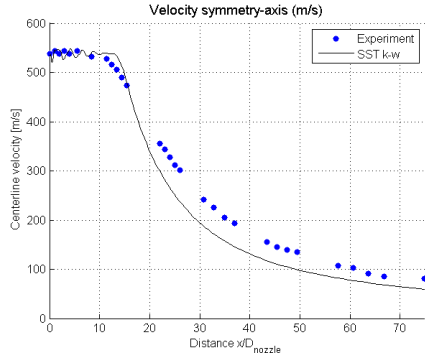
Figure 6 Validation Eggers
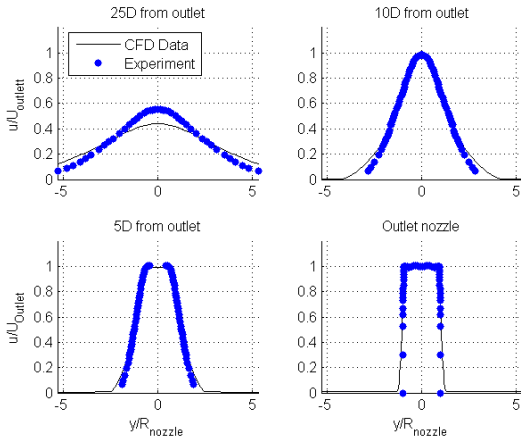
Figure 7 Radial velocity profiles at selected axial locations

In order to compare the nozzles with each other, global properties of the jet, such as force, mass flow rate and impinging pressure are calculated from the simulated flow fields. The mass flow rate induced by the pressure difference between the nozzle and surroundings can be calculated as

$$\dot{m}_{nozzle} = 2\pi \int_0^{\frac{D}{2}} \rho V_x r dr , \qquad (1)$$

where D is the nozzle diameter, V_x the axial velocity and ρ the density of the fluid. Since the flow is axisymmetric, integration is done only in the radial direction r . In order to be conform to the standards of industry, this mass flow rate is converted to a normal volumetric flow rate as

$$\dot{Q}_N = 3600 \left(2\pi \int_0^{\frac{D}{2}} \rho V_x r dr \right) \frac{RT_N}{p_N} , \qquad (2)$$

where R is the universal gas constant and T_N and P_N are the temperature and pressure at normal conditions respectively. The impact pressure of the jet is defined as

$$p_{impact} = \rho V_x^2 + \left(p - p_{surr} \right), \qquad (3)$$

where p is the static pressure. From this impact pressure, the impact force of the jet can be calculated as

$$F_{impact} = 2\pi \int_0^{R(x)} \left[\rho V_x^2 + \left(p - p_{surr} \right) \right] r dr , \qquad (4)$$

where the integration in de radial direction starts from the centerline up to a radius $R(x)$ where the velocity is 5% of the centerline velocity. By this definition, the entrained flow is also considered to contribute to the impact force. The converging diverging nozzle was adjusted to maximize the impact force at an input pressure of 5 bar$_g$. This could be done by changing the ratio between the area of the throat and the output. The exit pressure is than equal to the surrounding pressure [7].
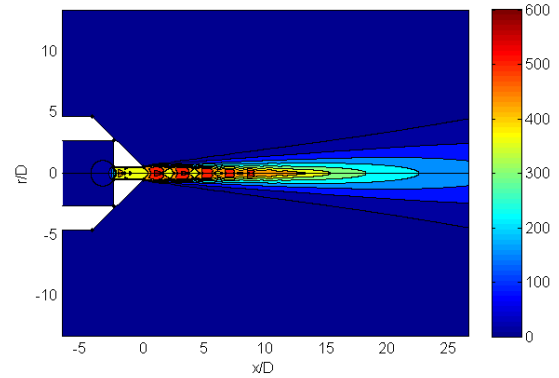

Figure 8 Velocity field of the jet (speed is given in m/s)

Figure 8 shows the velocity field of the stepped nozzle, and Figure 9 gives a closer look near the nozzle outlet. The nozzle shown in these figures is under expanded, i.e. the exhaust pressure is higher than the ambient pressure. Immediately at the exhaust, the jet flow is expanding as a result of the pressure difference with the surroundings. This effect results in shock diamonds, which can be found between 0 to 20 diameters from the exhaust. The jet flow compresses and expands alternately in that region. Further downstream, beyond 20 jet diameters, these shock diamonds become weaker and eventually they disappear. This is the region of interest for industrial applications as the nozzles used for blowing are mostly far away from their target.
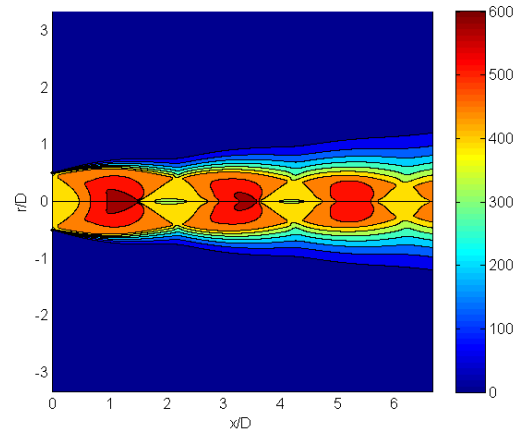
**Figure 9** Velocity field nozzle detail (speed is given in m/s)

The impact pressure field of the stepped nozzle is shown in Figure 9. Near the nozzle, the variation in impinging contact pressure due to the shock waves is clearly visible. Comparison of Figures 7 and 9 shows that the major contribution to the impact force comes from the static pressure difference and not as much from the momentum ρV_x^2, as regions with high velocity have a smaller impact pressure compared to regions with a low velocity. The impact pressure at the central axis of the jet after the region with shock diamonds is shown in Figure 10. This impact pressure decreases downstream due to the velocity decay of the jet as it spreads further downstream. After 60 nozzle diameters, the impact pressure is very similar for all nozzles as in this region the different jets evolve towards the self-similar state.
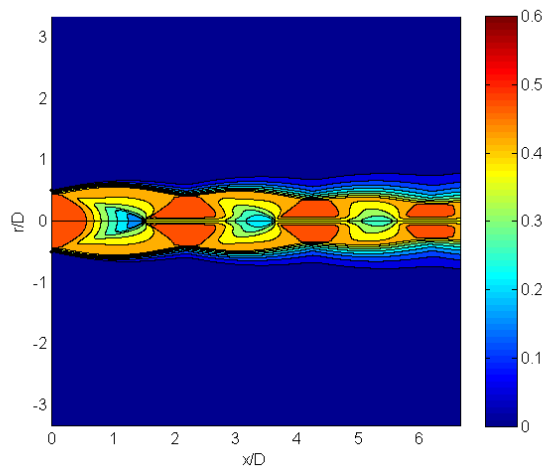
Figure 9 Impinging contact pressure (pressure in MPa)
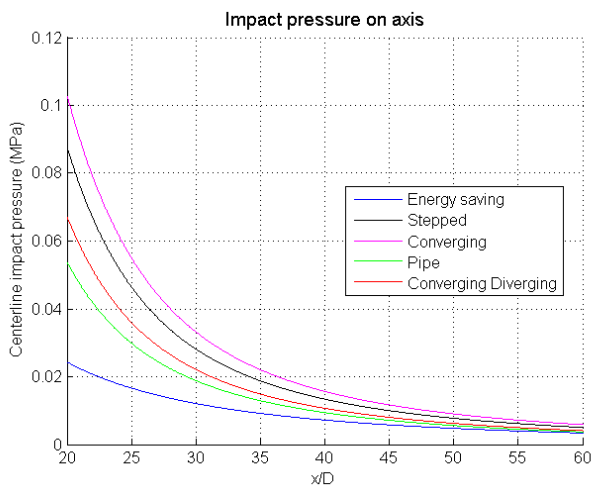
Figure 10 Impact pressure on the central axis at 5 bar$_g$

The input normal volumetric flow rates at 5 bar$_g$ are shown in Table 4. There is a large variation amongst the different nozzles. The energy saving nozzle has a lower volumetric flow rate than the stepped nozzle for more or less the same impact force. Inside the nozzle, it will entrain extra air from the

surroundings, because of the low pressure. For all nozzles, the convergent nozzle generates the largest impact force but the volumetric flow rate is the largest as well. Based on Table 4, if a compressed air network is available at 5 bar, the convergent nozzle should be chosen for maximum impact force, while a straight pipe should be chosen for minimal use of compressed air. As Table 4 shows, there is a large variation in flow rates and impact forces of the different nozzles, i.e. the nozzle with the lowest flow rate has also the lowest impact force and vice versa. Therefore it is important that we include the inlet volumetric flow rate when we are comparing the different impact forces. The most energy efficient nozzle is the one

Table 4 Impact force and volumetric flow rate

Type of nozzle	Q_N at 5 bar$_g$ (Nm³/h)	F_{impact} at 5 bar$_g$ (N)
Energy saving	5.73	1.03
Stepped	5.78	0.99
Pipe	4.89	0.80
Convergent	6.39	1.13
Convergent- divergent	4.68	0.82

with a large impact force for a small input volumetric flow rate, since the volumetric flow rate is directly proportional to the cost. The cost of one normal cubic meter of compressed air is between € 0.02 and € 0.03 on average in Europe [1]. This cost is an average and depends also on the compressed-air installation and energy prices. A specific impact force to include the volumetric flow rate is defined as

$$f_s = \frac{F_{impact}}{Q_N}. \tag{5}$$

Figure 11 shows the different specific forces for each nozzle in comparison with an ordinary straight pipe. It can be seen that the energy efficient nozzle has the best ratio between impact force and volumetric flow rate. The surrounding air which is entrained increases the impact force while the input volumetric flow rate stays the same. An ordinary pipe has the worst ratio of the five nozzles. The specific impact forces of the stepped, converging and converging-diverging nozzles are within two percent of each other, while the force volume ratio of the energy saving nozzle is five percent larger than the stepped nozzle. From Figure 11 it can be concluded that the use of a straight pipe is not very efficient for blowing applications. However due to its simple geometry it is the most widely used nozzle. If these nozzles were replaced by energy efficient nozzles, up to 10% in the use of compressed air would be saved.

Next to impact force for blowing application, entrainment can also be an important parameter in the use of compressed air. The ratio between the entrained air from the surroundings and the total mass flow rate of the jet is shown in Figure 12. The entrainment rate is defined as
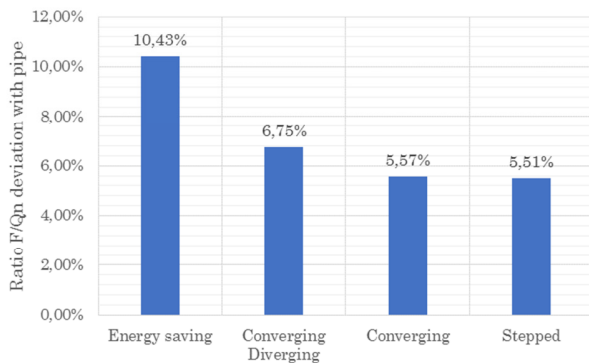
Figure 11 Specific impact force of the different nozzles at 5 bar$_g$

$$\varphi = 1 - \frac{\dot{m}_{nozzle}}{\dot{m}_{total}}, \qquad (6)$$

where the total mass flow rate is the sum of the mass flow rate through the nozzle and the mass flow rate of the entrained air. As expected the energy saving nozzle has indeed the largest entrainment rate. Near the nozzle, already around 50% of the total mass flow comes from entrained air. This difference decreases further downstream as the entrainment rate for the different nozzles is similar as the jets evolve towards the self-similar state.
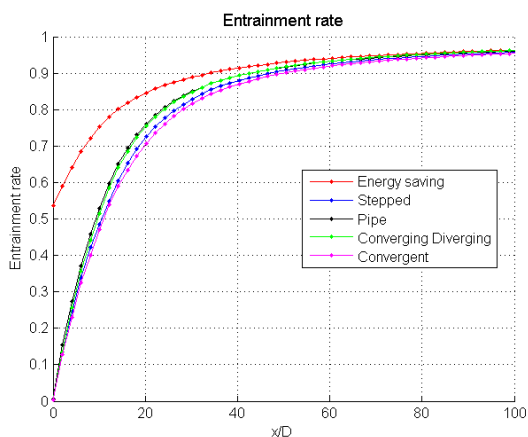
Figure 12 Entrainment rates of the different nozzles.

CONCLUSION

In this study a comparison of 5 different nozzles used in industrial blowing applications is made. In order to compare the different nozzles with each other, general properties of the jets, like the total impact force, the impact pressure and the entrainment rate were obtained from the simulations. It was shown that the stepped, converging and converging-diverging nozzles use around 5% less compressed air for the same impact force compared to a straight pipe. A special designed energy efficient nozzle uses even 10% less air. This nozzle utilizes entrained air form the surrounding to decrease the mass flow

used and is therefore also suited for industrial applications were entrainment is important.

ACKNOWLEDGMENTS

REFERENCES

[1] R. v. O. N. RVO, „Best Practice Document Persluchtinstallaties," 2014.

[2] E. Deliège, "Benchmark Perslucht NRK 2003," Federatie NRK, Arnhem, 2003.

[3] P. Radgen, Compressed Air Systems in the European Union, Stuttgart: Fraunhofer ISI, 2001.

[4] U. D. o. Energy, Improving Compressed Air System Performance, Washington: U.S. Departement of Energy, 2003.

[5] F. Schoutsen, "Energy Saving," Wommelgem, 2014.

[6] T. J. Tipnis, "Effects of Upstream Nozzle Geometery on Rectangular Free Jets," Cranfield University, Cranfield, 2009.

[7] J. Ostlund, "Flow Processes in Rocket Engine Nozzles with Focus on Flow Separation and Side-Loads," Kungl Tekniska Hogskolan, Stockholm, 2002.

[8] R. Ghias, "Simulation of flow through supersonic cruise nozzle: A validation study," NASA Langley Research Center, Hampton, 2011.

[9] H. Ogawa, "Physical Insight into nozzle flow behaviour of axisymmetric scramjets for acces-to-space via Design Optimisation," Centre for Hypersonics, School of Mechanical and Mining Engineering, The University of Queensland, St. Lucia Brisbane, Brisbane, 2012.

[10] J. Eggers, "Velocity Profiles and Eddy Viscosity Distributions Downstream of a Mach 2.22 Nozzle Exhausting to Quiescent Air," NASA, Langley Research Center, 1966.

[11] R. B.V, "Unsteady Computation of Over-Expanded Flow in a Convergent Divergent Nozzle," in *International Conference on Computing, Communications, Systems and Aeronautics, ICCCSA-2012*, Salvador de Bahia, 2012.

EFFECT OF PREHEATING ON THE FLOW CHARACTERISTICS OF SWIRLING MULTICOAXIAL JETS IN AN EXPANDED CONFINEMENT

V.K. Patel[1*], S.N. Singh[2] and V. Seshadri[3]

[1]Assistant Professor, Department of Applied Mechanics, MNNIT Allahabad (INDIA)
[2]Professor, Department of Applied Mechanics, Indian Institute of Technology Delhi (INDIA)
[3]Professor (Retd.), Department of Applied Mechanics, Indian Institute of Technology Delhi (INDIA)
[*]Corresponding Author, E-mail: vivek@mnnit.ac.in

ABSTRACT

Swirling multicoaxial jets consisting of one central jet and two coaxial annular jets increase the combustion efficiency in gas turbine combustors. The present work is carried out to understand the effect of preheating the fuel jet in the multicoaxial jet arrangement. This has been done using CFD code FLUENT. Before carrying out computations, the CFD code was validated against the experimental data. It was found that the SST k-ω model gives the best agreement with experimental results. Computations have been carried out by heating either the central jet or annular jet-1. The predicted results are plotted in the form of axial velocity profiles at different axial locations of the test section, contours of axial velocity, turbulent intensity, temperature profiles, central line axial velocity and static pressure. It is concluded that the effect of heating in individual jets with the optimum swirl combination enhances the mixing process. Further heating of annular jet-1 is found to be more effective in enhancing the mixing and ensuring a comparatively bigger central recirculation zone in the radial direction.

Keywords: Multicoaxial Jets, Heated Jet, Swirling flows, CFD, GT Combustor, CRZ and Mixing of Jets

INTRODUCTION

Coaxial jets having additional co-annular jets are termed as multicoaxial jets. Mixing of these jets in an expanded confinement is a very complex phenomena and challenging area of research. It finds many applications in the area of aerospace and other engineering devices. One of its very important applications is the mixing of the fuel with air in the gas turbine combustors. A gas turbine combustor working under fuel rich mode produces a very stable and undisturbed flame. However, when the fuel and air ratio decreases, the flame starts losing its stability and then the proper mixing of these jets is desirable to make the flow stable for the stability of flame (Akselvoll & Moin, 1996). One of the successful techniques of flame stabilization is to produce a central recirculation zone (CRZ) at the exit of the jets. Acharya (1954) was the first who studied the effect of temperature difference in the jets on the turbulent mixing of confined coaxial jets. He found that the mixing of jets is significantly influenced by temperature ratios. Tsuji et al. (2003) studied flame characteristics by preheating the fuel, air or both by recycling the heat from combustor products. They found that the heating of jets is an effective technology not only for low calorific fuel combustion but also for fuel conservation. A very recent study on the effect of blockage of heated coaxial jets has been reported by Patel et al. (2013, 2014) which shows the

adequacy of k-ω model for the analysis of swirling heated coaxial jets. It also demonstrates the positive effect of heat addition with blockage on the formation of central recirculation zone (CRZ).

NOMENCLATURE

u_i	[m/s]	Velocity in i^{th} direction
S_m		Mass added to continuous phase
P	[Pa]	Static pressure
ρg_i		Gravitational body force
F_i		External body force
H	[Joule]	Enthalpy
k'	[W/(m·K)]	Isotropic thermal conductivity
D_ω		Cross-diffusion modification term
G_k		Generation of turbulent kinetic energy due to the mean velocity gradient
G_ω		Generation of ω
S_k		User defined source terms
S_ω		User defined source terms
Y_k		Dissipation of k
Y_ω		Dissipation of ω
T	[°C]	Temperature
x	[m]	Variable axial distance along the length of the flow domain
d	[m]	Diameter of the jet
r	[m]	Variable radial distance
R	[m]	Radius of jet
AJ		Annular Jet
CJ		Central Jet
CRZ		Central Recirculation Zone

Special characters

ρ	[kg/m^3]	Density
τ_{ij}	[N/m^2]	Deviatoric stress tensor
Γ_k		Effective diffusivity of k
Γ_ω		Effective diffusivity of ω
Δ		Difference between two quantities

Subscripts

o	Outer jet
i	Inner jet

MATHEMATICAL FORMULATION AND CFD ANALYSIS

The governing equations (continuity, momentum and energy equation) for steady and incompressible turbulent flow are given as:

$$\frac{\partial}{\partial x_i}(\rho u_i) = S_m \tag{1}$$

$$\frac{\partial}{\partial x_j}(\rho u_i u_j) = \frac{\partial P_i}{\partial x_i} + \frac{\partial \tau_{i,j}}{\partial x_j} + \rho g_i + F_i + \frac{\partial}{\partial x_j}\left(-\overline{\rho u_i' u_j'}\right) \tag{2}$$

$$\frac{\partial}{\partial x_i}(\rho u_i H) = \frac{\partial}{\partial x_j}\left(k'\frac{\partial T}{\partial x_j}\right) + \frac{\partial}{\partial x_j}(\tau_{ij} u_i) \tag{3}$$

The last term in the second equation is the Reynolds stresses. For closure solution, term $-\overline{\rho u_i' u_j'}$ in momentum equation has to be modeled. *Boussinesq hypothesis* is used to relate the Reynolds stresses with the mean velocity gradient. Commercial CFD code FLUENT has been used for the present study. *SST k-ω turbulent model* is selected for the studies. The *SST k-ω* model is based on transport equations for turbulence kinetic energy (k) and the specific dissipation rate (ω). where, specific dissipation rate (ω) is the ratio of ε to k. The transport equations for the turbulence kinetic energy k and specific dissipation rate ω are given as (Fluent, 2006):

$$\frac{\partial}{\partial x_i}(\rho k u_i) = \frac{\partial}{\partial x_j}\left(\Gamma_k \frac{\partial k}{\partial x_j}\right) + \tilde{G}_k - Y_k + S_k \tag{4}$$

$$\frac{\partial}{\partial x_i}(\rho \omega u_i) = \frac{\partial}{\partial x_j}\left(\Gamma_\omega \frac{\partial \omega}{\partial x_j}\right) + G_\omega - Y_\omega + D_\omega + S_\omega \tag{5}$$

A second order discretization scheme is used for all governing equations. The pressure and velocity Coupling have been established by using the SIMPLE scheme (Patankar, 1980). Convergence of solution is established by ensuring that all the residual terms are less than 10^{-6}.

DETAILS OF GEOMETRY AND FLOW DOMAIN

In the present study, a flame stabilization method is proposed to generate adequate mixing of the jets. For the sake of simplicity, all the jets of multicoaxial jets have been treated as air jets and chemical reaction has not been considered in the flow analysis. The flow domain has been modeled based on the geometry of test-section used by Patel (2014, Figure 1) in his experimental studies. "GAMBIT" is used in the present study for the modeling and generation of mesh. A sufficiently fine mesh is provided in the area of shear layer and at the axis of the confinement, where the formation of CRZ is taking place. Grid independency tests have been done for all of the cases and approximately 0.56 million meshes have been used for the present study.
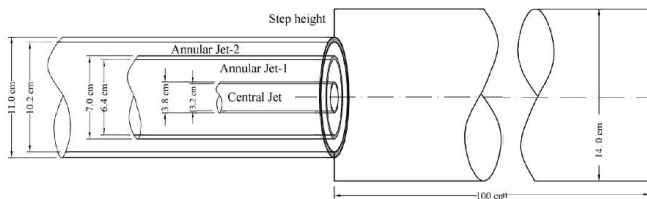

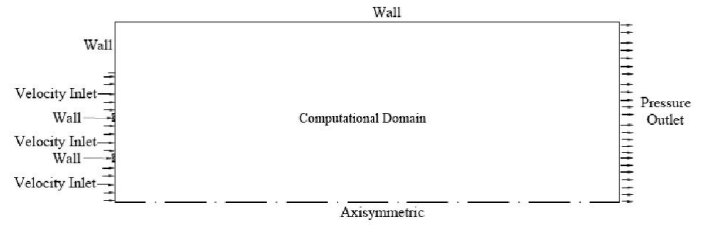**Figure 1** Geometry of multicoaxial jets

Figure 2 Boundary conditions

The possible fuel jet (central jet or annular jet-1) has been heated upto 150°C above the atmosphere temperature. 45° swirl in counter flow arrangement have been provided in all the jets. The expansion ratio of the confinement has been kept as 1.4 and the average inlet velocity of the central jet, annular jet-1 and annular jet-2 have been specified as 13.5 m/s, 14.5 m/s and 28 m/s, respectively. All the velocities are fed at the inlet of the jets in the form of 'user defined velocity profiles' based on experimental measurements taken at the exit of these jets (Patel, 2014). The exit of the flow domain is defined as 'Pressure outlet' boundary condition and the walls in the flow domain are assigned as 'no-slip' boundary condition (Figure 2). Before carrying out different runs, the CFD code has been validated against the experimental data given by Patel (2014) using different turbulence models. Based on the comparison, it was seen that *SST k-ω* model gives the best matching. After identification of the turbulence model, several runs have been made using CFD code 'FLUENT' by varying the temperature of the jet (central or annular jet-1) ranging from 30°C to 150°C above the atmospheric temperature.

RESULTS AND DISCUSSION

Effect of heat addition on the flow characteristics of swirling multicoaxial jets have been predicted using CFD code FLUENT. For this, the experimentally measured velocity profiles are modified for keeping mass flow rate constant and fed at the inlets of the test section. The corresponding temperature and optimum swirl (Patel, 2014) have also been defined at the inlet of the test section. The predicted results are plotted in the form of axial velocity profiles at different axial locations of the test section, contours of axial velocity, turbulent intensity and temperature, central line axial velocity and wall static pressure.

Flow Characteristics for Heated Central Jet:

To establish the effect of heated central jet, the central jet (CJ) inlet temperature is varied above atmospheric temperature in the interval of 30°C. Five flow cases, i.e. $\Delta T=30°$, $\Delta T=60°$, $\Delta T=90°$, $\Delta T=120°$ and $\Delta T=150°C$, have been analyzed for the present study. The predicted results are plotted in the form of axial velocity profiles at different axial locations of the test section (Figure 3 and Figure 4).

The axial velocity plot at $x/d_0=0.125$ shows the increase in velocity of central jet with increase in temperature. This increment is due to decrease in density of fluid in central jet because velocity needs to be increased to ensure constant mass flow ratio in jets. It is seen that at $x/d_0=0.25$, the central jet drags the annular jet-1 collectively as the temperature of central jet increases and hence tries to fill the dip between these jets faster.

This is due to high centrifugal force and thermal diffusion of the central jet.
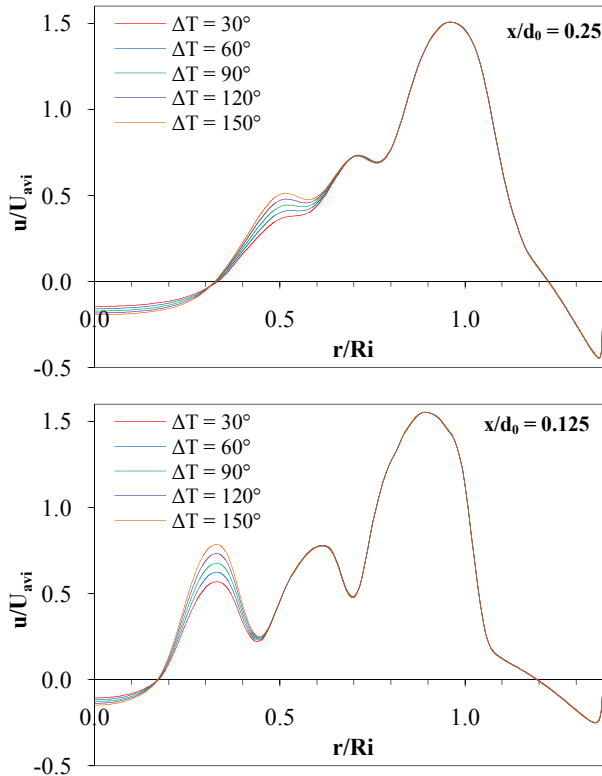
Figure 3 Comparison of axial velocity at two axial locations of test section for various temperatures in central jet

(a) $\Delta T=30°C$

(b) $\Delta T=90°C$

(c) $\Delta T=150°C$
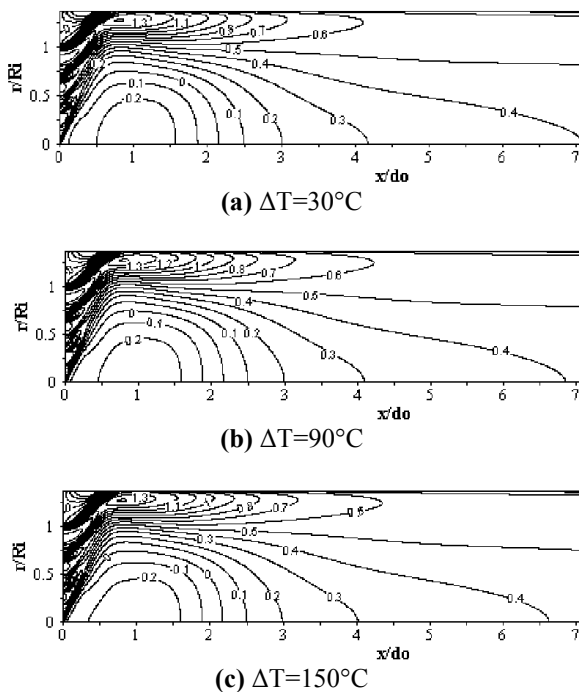
Figure 4 Iso-contours of normalized axial velocity at different ΔT in central jet

Because of this enhanced shearing action, a slightly higher turbulent intensity is observed near these shear layers for higher temperature case (Figure 5), but these shear layers are not significantly strong enough to increase mixing considerably in the near flow field. Therefore, the axial velocity after location $x/d_0=0.5$ is almost similar (Figure 4) and turbulent intensity in most of the area of test section is observed to be identical for all the cases (Figure 5). However, in Figure 3, the axial velocity contour level -0.2 seems to be farther upstream as the temperature increases. This may be due to increase in tangential velocity that produces higher centrifugal force for highly heated fluid in central jet.

(a) $\Delta T=30°C$

(b) $\Delta T=90°C$

(c) $\Delta T=150°C$
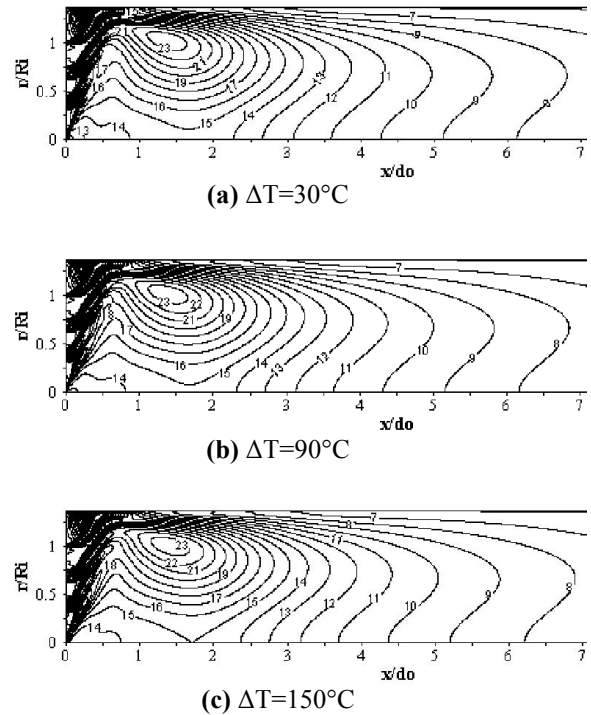
Figure 5 Iso-contours of turbulent intensity at different ΔT in central jet

Figure 6 shows the temperature contours for various temperatures in central jet. Observation shows that the increase in central jet temperature heats only small areas ahead to the central jet, whereas, the temperature of other areas of the test section only changes slightly. The observation of central line axial velocity plot (Figure 7) illustrates slight decrease in velocity, from location $x/d_0=0$ to $x/d_0=0.7$, with increase in central jet temperature. However, after location $x/d_0=0.7$, no significant effect is observed in the centerline axial velocity.

Figure 8 demonstrates the wall static pressure plot along the length of the test section confinement wall. Like centerline axial velocity plot, no significant effect of increase in temperature of central jet is observed at the wall static pressure along the test section wall.

(a) $\Delta T=30°C$

(b) $\Delta T=90°C$

(c) $\Delta T=150°C$
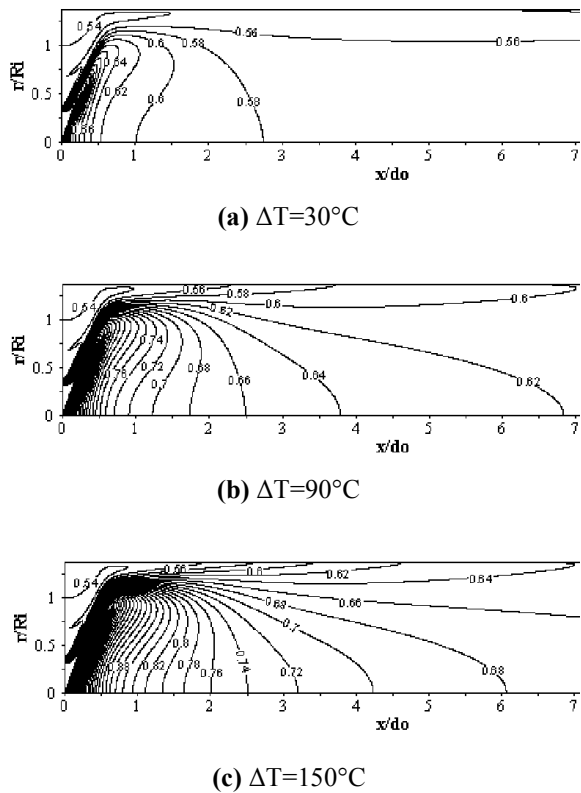
Figure 6 Iso-contours of normalized temperature at different ΔT in central jet
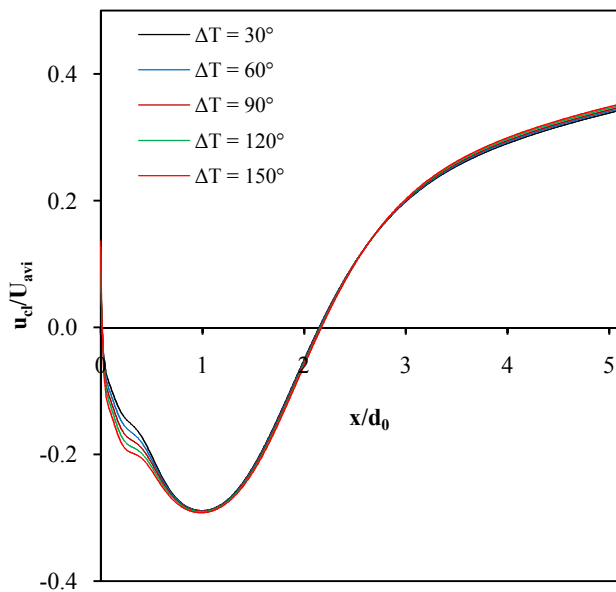
Figure 7 Comparison of centre line axial velocity along the length of test section for various temperatures in central jet
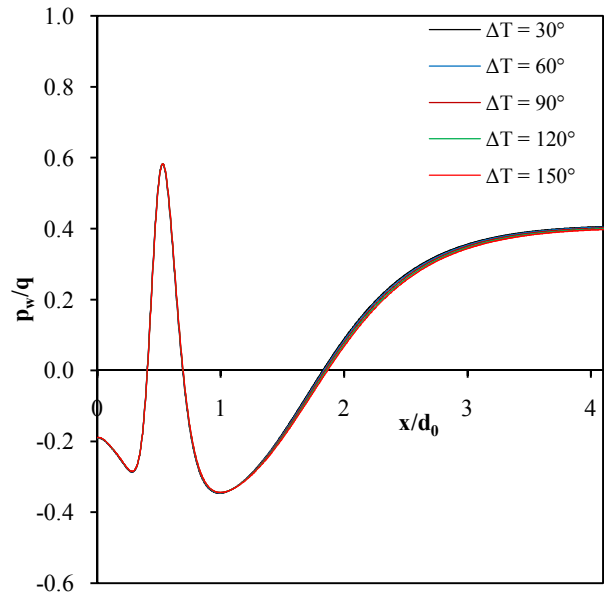
Figure 8 Comparison of wall static pressure along the length of test section for various temperatures in central jet

Flow Characteristics for Heated Annular Jet-1:

To study the effect of heated annular jet-1 on the flow characteristics of swirling multicoaxial jets exhausting in an expanded confinement, temperature of annular jet-1 is varied in the same way as was done for central jet and same five cases of temperature have been used for the investigations. Figure 9 illustrates the axial velocity plot at different axial locations of the test section. The axial velocity profiles at $x/d_0=0.125$ indicate that the axial velocity of annular jet shows higher magnitude with increase in temperature (Figure 9). The reason of this increment is same as already discussed for central jet cases. It is observed that, as the temperature of annular jet-1 increases, it drags both the adjacent jets (CJ and AJ-2) collectively and tries to fill the dip between jets faster. It is also observed that the negative velocity in the profiles ($x/d_0=0.5$ and 1) decreases as temperature of AJ-1 increases. This is due to increase in tangential velocity and centrifugal force in annular jet-1 with increase in temperature.
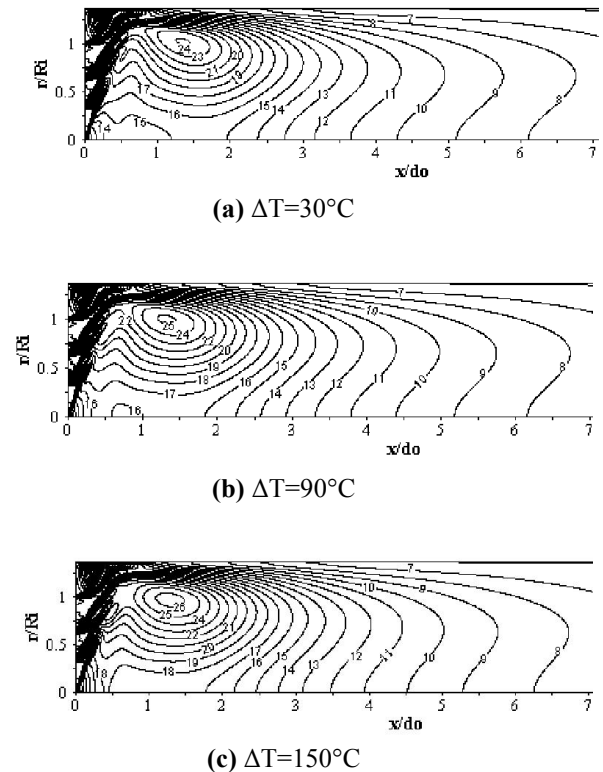
Figure 10 illustrates the axial velocity contour plots at various temperatures in annular jet-1. The observation shows that the negative velocity magnitude has increased considerably in the near flow field because of the faster shearing between the jets at higher temperature. This increase in negative velocity develops higher recirculation in the centre of the test section that causes intensive mixing of the jets. This intensive mixing of the jets is one of the most important requirements of real combustor for fuel and air mixing. It is also seen from Figure 10 that the contour level 0.4 shifts towards inlet with increase in annular jet-1 temperature, and after $x/d_0 \approx 5$, the contour level 0.5 can be observed everywhere in the test section ($\Delta T =150°$, Figure 10b). It shows the flow uniformity in downstream of the test section and also exhibits higher mixing in the near flow field.
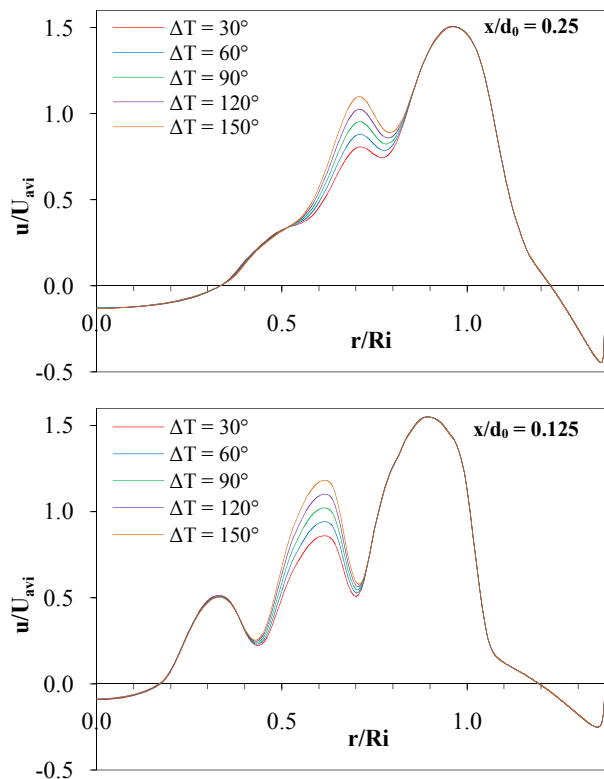
Figure 9 Comparison of axial velocity at two axial locations of test section for various temperatures in annular jet-1

(a) $\Delta T = 30°C$

(b) $\Delta T = 90°C$

(c) $\Delta T = 150°C$

Figure 10 Iso-contours of normalized axial velocity at different ΔT in Annular Jet-1

(a) $\Delta T = 30°C$

(b) $\Delta T = 90°C$

(c) $\Delta T = 150°C$

Figure 11 Iso-contours of turbulent intensity at different ΔT in Annular Jet-1

The observation of turbulent intensity at different temperatures (Figure 11) demonstrates the increase of turbulent intensity in the near flow field with increase in temperature. This increment in turbulent intensity could be due to the thermal diffusion of the annular jet-1. At $\Delta T = 30°C$, the maximum turbulent intensity is observed up to 24%, whereas, at $\Delta T = 150°C$, this value increases up to 26%. Iso-contours of temperature at different ΔT are plotted in Figure 12. It shows that the increase in annular jet-1 temperature heats both sides of the jet and increases the temperature of neighboring jets. In this way, the entire area of the near flow field except wall region gets heated properly. This is very significant for flame stabilization and achieving uniform temperature in real combustors. The central line axial velocity and wall static pressure are plotted in Figure 13.

The magnitude of negative velocity from $x/d_0=0$ to $x/d_0=2.2$ in central line axial velocity plot increases with the increase in temperature (Figure 13). All the flow cases show same centre line axial velocity at $x/d_0=2.25$ and moreover overall profile shows slightly higher velocity throughout the test section for higher value of ΔT. The wall static pressure plot along the length of the test section (Figure 14) shows relatively reduced magnitude with increase in annular jet-1 temperature and this is more considerable after $x/d_0=1$. This may be due to increase in velocity magnitude in CRZ.

(a) ΔT=30°C

(b) ΔT=90°C

(c) 150°C
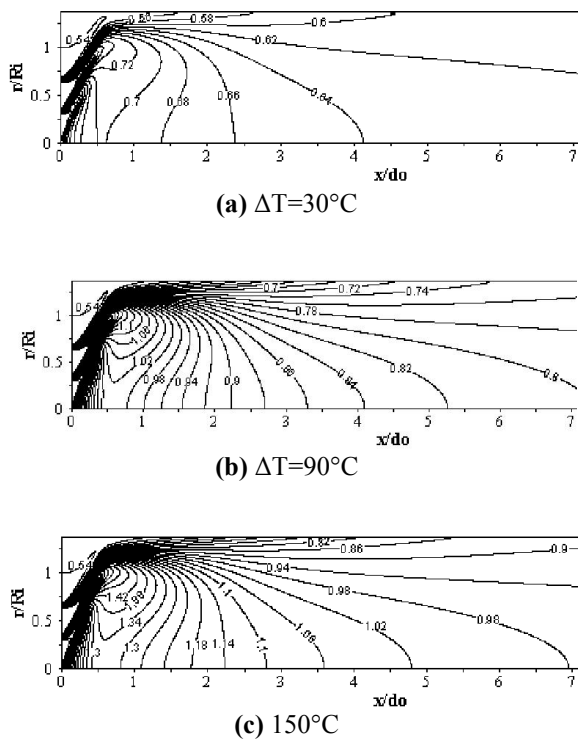
Figure 12 Iso-contours of normalized temperature at different ΔT in Annular Jet-1
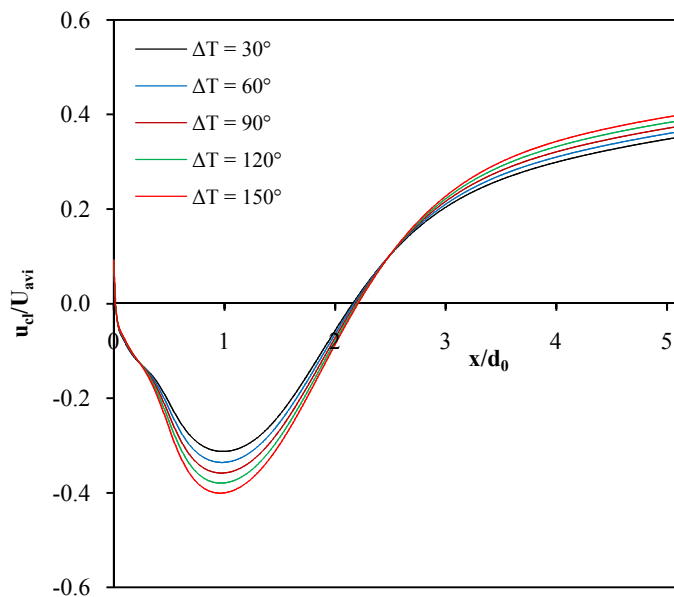

Figure 13 Comparison of centre line axial velocity along the length of test section for various temperatures in Annular Jet-1

CONCLUSIONS

Investigations on the effect of heated fuel jets on the swirling multicoaxial jets have been done for the prediction of mixing of the fuel-air jets. The present study proves the capability of *SST* k-ω *model* for prediction of heated swirling multicoaxial jets. After studying both the flow cases of temperature variation in central jet and annular jet-1, it is concluded that the increasing temperature in annular jet-1 increases turbulence in the near flow field and hence enhances the mixing between the jets. Therefore, it is established that the annular jet-1 is the appropriate jet for heating in a real combustor and should be the fuel jet.
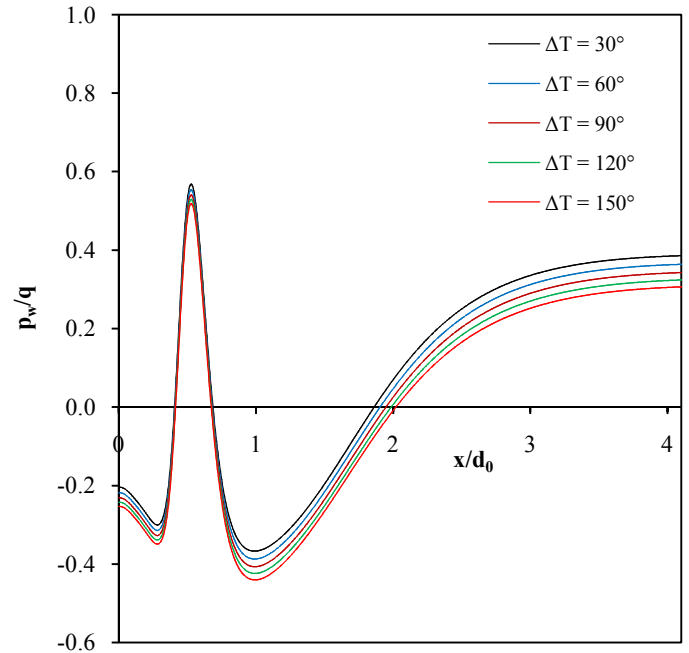
Figure 14 Comparison of wall static pressure along the length of test section for various temperatures in Annular Jet-1

REFERENCES

[1] Acharya, Y.V.G., Momentum Transfer and heat Diffusion in the Mixing of Coaxial Turbulent Jets Surrounded by a Pipe, 1954, *Excelsior*, India.

[2] Akselvoll, K., and Moin, P., Large Eddy Simulation of Turbulent Confined Coaxial Jets, *Journal of Fluid Mechanics*, 1996, Vol. 315, pp. 387-411.

[3] Tsuji, H., Gupta, A. K., Hasegawa, T., Katsuki, M., Kishimoto, K., and Morita, M., High Temperature Air Combustion. From Energy Conservation to Pollution Reduction, 2003, CRC Press.

[4] FLUENT 6.3, *User Guide Fluent Inc.*, 2006, Lebanon, NH 03766, USA.

[5] Patankar, S. V., Numerical Heat Transfer and Fluid Flow, 1980, Taylor and Francis Publication.

[6] Patel, V.K., Singh, S.N. and Seshadri, V., Effect of Blockage and Location on Mixing of Swirling Coaxial Jets in a Non-expanding Circular Confinement, *International Journal of Turbo & Jet Engine*, 2013, Vol. 30, Issue 2, pp. 153-172.

[7] Patel, V. K., Singh, S. N. and Seshadri, V., Effect of Blockage and its Location on the Flow Characteristics of Heated Swirling Coaxial Jets in a Non-expanding Confinement, *5th International and 41st National Conference on Fluid Mechanics & Fluid Power,* 12-14 December, 2014, IIT Kanpur, Ref. No. 234.

[8] Patel, V. K., Studies on the Flow Characteristics of Heated Coaxial and Multicoaxial Jets, 2014, *Ph.D. Thesis*, IIT Delhi, New Delhi, India.

FLUID-STRUCTURE INTERACTION OF A FREE-TO-ROLL SLENDER BODY OF REVOLUTION AT HIGH ANGLES OF ATTACK

Degani D.* and Gottlieb O.
*Author for correspondence
Department of Mechanical Engineering,
Technion-Israel Institute of Technology,
Haifa 32000, Israel
E-mail: degani@technion.ac.il

ABSTRACT

The current work investigates numerically the effect of unsteady rolling moments which are generated when a slender body of revolution is placed in a wind tunnel at a high angle of attack and is allowed to rotate around its longitudinal axis of symmetry. The resistance to the roll moment is represented by a linear torsion spring and equivalent linear damping representing friction in the bearings. The body is subjected to a three-dimensional, compressible, laminar flow. The full Navier-Stokes equations are solved using the second-order implicit finite difference Beam-Warming scheme, adapted to a curvilinear coordinate system, whereas the coupled structural second order equation of motion for roll is solved by a fourth-order Runge-Kutta method. The body consists of a 3.5-diam tangent ogive forebody with a 7.0-diam long cylindrical afterbody extending aft of the nose-body junction to x/D = 10.5. We describe in detail the investigation of three angles of attack, $20°$, $40°$ and $65°$, at Reynolds number of 30,000 (based on body diameter) and Mach number of 0.2. For each angle of attack the free-to-roll configuration portrays a distinct and different behavior pattern, including periodic and quasiperiodic oscillations. Depending on structure characteristics and flow conditions even a small rolling moment coefficient at the relatively low angle of attack of $20°$ may lead to large amplitude resonant roll oscillations.

NOMENCLATURE

a_∞	=	speed of sound
C_{Mx}	=	rolling-moment coefficient
C_{My}	=	pitching-moment coefficient
C_{Mz}	=	yawing-moment coefficient
D	=	cylinder diameter
D_ϕ	=	linear damping
d_ϕ	=	dimensionless damping
$\hat{E}, \hat{F}, \hat{G}$	=	inviscid flux vectors
$\hat{E}_v, \hat{F}_v, \hat{G}_v$	=	viscous flux vectors
g	=	gravity
h	=	disturbance height
I_{xx}, I_{yy}	=	moments of inertia
K_ϕ	=	torsion stiffness coefficient
k_ϕ	=	dimensionless stiffness
M_∞	=	free stream Mach number
$\hat{Q}$	=	vector of dependent flow variables
$q_j = (\theta, \psi, \phi)$	=	generalized coordinates
Re	=	Reynolds number
T	=	rescaled dimensionless time
t	=	time
x, y, z	=	coordinate system
X, Y, Z	=	inertial coordinate system
α	=	angle of attack
γ	=	dimensionless inertia
θ, ψ, ϕ	=	Euler angles
λ	=	dimensionless gravity
μ	=	mass ratio
ξ_ϕ	=	damping ratio
ξ, η, ζ	=	computational coordinate system
ρ	=	density
τ	=	dimensionless time
Φ	=	disturbance circumferential roll angle
ω_ϕ	=	natural frequency

INTRODUCTION

The onset of vortex asymmetry on the forebody of an aircraft maneuvering at large angles of attack can generate unwanted yawing moments, which can lead to departure from controlled flight. This phenomenon is typified by the vortex asymmetry observed in the flow around slender bodies of revolution at large incidence. Even though the geometry of the latter is simple, the flow around it is intricate and even early wind tunnel experiments have indicated that measurements were not repeatable. This can be partly answered by the explanation that the body is not really symmetric and at high angle of attacks this is enough to trigger a change. The flow field can be so

unstable that even upcoming turbulence [1] or a small upstream disturbance [2] can change the flow abruptly. Over the years it has been shown that these side forces can be altered by changing the body roll angle [3] or by placing small irregularities near the body tip [4]-[7]. Other researchers have investigated the influence of tip vortices on the behavior of the flow over wings of the case of slender forebody-wing combinations [8]-[9]. Ericsson [10] speculated that the forebody vortices at a high angle of attack can induce wing rock or even body rock [11] in the case of a slender body (based on the experiments of Keener et al. [12]). Yoshinaga et al [13] demonstrated experimentally that the asymmetric vortices emanating from a cone-cylinder body at a high angle of attack can initiate and sustain free coning motion of the body. Recently, Wang et al [14] repeated wing-rock experiments of a free-to-roll slender forebody-delta wing configuration and also speculated that wing rock is induced by tip vortices of the pointed forebody. Nevertheless, none of these publications present a verified mechanism how this interaction really works. However, the influence of the rolling moments acting on the forebody due to the viscous forces induced by the unsteady asymmetric vortices has not been noticed or investigated to-date. These moments, relatively very small, can force rotation of the forebody and therefore have a significant effect on vehicle flight control. Moreover, in the case of a nonlinear interaction between the flow and the structure these rolling moments can play a significant role.

The current work investigates numerically the effect of rolling moments which are generated when a slender body of revolution is placed in a wind tunnel at a high angle of attack and is allowed only to rotate around its longitudinal axis of symmetry. The resistance to roll is modeled by a linear torsion spring and linear equivalent damping due to friction in the bearings. Thus, the structure is represented by a linear second-order ordinary differential equation. The body is subjected to a three-dimensional, compressible, laminar flow. The full Navier-Stokes equations are solved using the second-order implicit finite difference Beam-Warming scheme, adapted to a curvilinear coordinate system, whereas the coupled structural equation is solved by a fourth-order Runge-Kutta method.

We describe in detail the investigation of three angles of attack: $20°$, $40°$ and $65°$ at Reynolds number of 30,000 (based on body diameter) and Mach number of 0.2. The body consists of a 3.5-diam tangent ogive forebody with a 7.0-diam long cylindrical afterbody extending aft of the nose-body junction to $x/D = 10.5$. For all cases a small perturbation is placed near the tip of the body at a circumferential angle of $90°$.

PROBLEM FORMULATION

Flowfield: Governing equations and numerical algorithm
The conservation equations of mass, momentum, and energy can be represented in a flux-vector form as:

$$\partial_\tau \hat{Q} + \partial_\xi \hat{E} + \partial_\eta \hat{F} + \partial_\zeta \hat{G} =$$

$$\frac{1}{Re}\left(\partial_\xi \hat{E}_v + \partial_\eta \hat{F}_v + \partial_\zeta \hat{G}_v\right) \qquad (1)$$

where τ is the dimensionless time and the independent spatial variables ξ, η and ς are chosen to map a curvilinear body-conforming grid into a uniform computational space. In Eq. (1), $\hat{Q}$ is the vector of dependent flow variables; $\hat{E} = \hat{E}(\hat{Q})$, $\hat{F} = \hat{F}(\hat{Q})$, and $\hat{G} = \hat{G}(\hat{Q})$ are the inviscid flux vectors; and the terms $\hat{E}_v$, $\hat{F}_v$ and $\hat{G}_v$ are fluxes containing derivatives of the viscous terms. A dimensionless form of the equations is used throughout this work[15]. The implicit Beam-Warming finite difference algorithm[16] which is second-order accurate both in time and space, is adapted to solve Eq. (1) in a three-dimensional curvilinear coordinate system [17], where all viscous terms are retained [18].

Computations were performed for subsonic flows over an ogive-cylinder body of diameter D, which consists of 3.5-diameter tangent ogive forebody with a 7.0-diameter cylindrical afterbody (see Fig. 1). The grid consisted of 120 equispaced circumferential planes extending completely around the body. In each circumferential plane, the grid contained 50 radial points between the body surface and the computational outer boundary and 60 axial points between the nose and the rear of the body. An adiabatic no-slip boundary condition was applied at the body surface, and undisturbed freestream conditions were maintained at the computational outer boundary. An implicit periodic continuation condition was imposed at the circumferential edges of the grid, and at the downstream boundary, a simple zero-axial-gradient extrapolation condition was applied.

Structure: Governing equation and numerical algorithm
The ogive-cylinder body is considered rigid and is only allowed to rotate about its longitudinal axis of symmetry. The resistance to the roll is represented by a linear torsion spring and linear equivalent damping due to friction in the roll bearings.
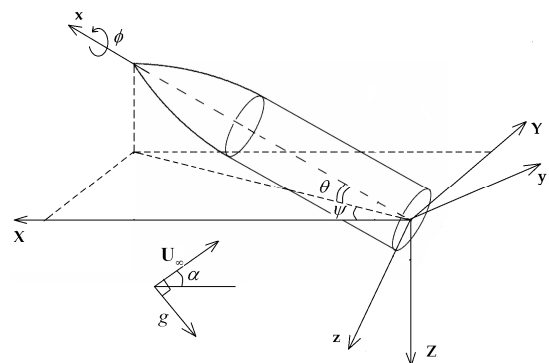

Figure 1. Body and coordinate systems.

We make use of a Lagrangian formulation [19] where the generalized coordinates are the Euler angles defined in Fig.1 for pitch, yaw, and roll respectively: $q_j = (\theta, \psi, \phi)$. We limit the body to move only in roll direction ϕ and obtain the following equation for $\phi_{\tau\tau}$ (see [20])

$$\phi_{\tau\tau} = \frac{1}{\gamma} \left(\mu C_{Mx} - k_\phi \phi - d_\phi \phi_\tau \right) \qquad (2)$$

where $\tau = a_\infty t / D$ is the dimensionless time and, C_{Mx} is the roll aerodynamic moment coefficient in the moving body reference frame (x,y,z).

The dimensionless parameter groups in the equation of motion include stiffness (k), damping (d), mass ratio (μ) and inertia (γ):

$$k_\phi = \frac{K_\phi}{a_\infty^2 D^{-2} I_{yy}}, \; d_\phi = \frac{D_\phi}{a_\infty D^{-1} I_{yy}}, \; \mu = \frac{\rho_\infty D^5 M_\infty^2}{2 I_{yy}}, \; \gamma = \frac{I_{xx}}{I_{yy}} \quad (3)$$

where K_ϕ and D_ϕ are the torsion stiffness and damping coefficients in the ϕ direction and I_{xx}, I_{yy} are the respective moments of inertia of the body.

Linearization of the equation of motion enables computation of the dynamical system natural frequency ($\omega_\phi = \sqrt{k_\phi / \gamma}$) and the corresponding linear damping ratio ($\xi_\phi = d_\phi / 2\gamma\omega_\phi$).

The roll equation of motion (2) can be rescaled again by $T = \tau / \sqrt{\mu / \gamma}$ to yield:

$$\phi_{TT} = C_{Mx} - \kappa\phi - \delta\phi_T \qquad (4)$$

which is clearly governed by two parameters: the ratio between the torsion stiffness and mass ($\kappa = k_\phi / \mu$) and the linear damping ratio ($\xi_\phi = \delta / 2\sqrt{\kappa}$).

The structural equation is solved using the explicit fourth-order Runge-Kutta method.

Flow–Structure coupling algorithm: Since the structural motion and the flow field are unknown, at each time step the flow solver and the structure calculations are loosely coupled (e.g., Refs. [21] - [22]). The coupling procedure includes the following:
1) The variables at new time level n + 1 of the flow and structural equations are initially set to be the known values at time level n. Using the flow field solution the aerodynamic forces and moments acting on the solid body are calculated.
2) The new Euler angles of the body are determined by solving the structural equations.

3) The grid is regenerated and the grid velocity (time metrics) at each node point is calculated according to the updated structural position.
4) The flow field is calculated by solving the Navier-Stokes equations for the updated grid and structural position.
5) Using the flow field solution the aerodynamic forces and moments acting on the solid body are calculated.
6) The maximum residuals for both solutions of the flow and the structural equations are checked. If the maximum residuals are greater than the prescribed convergence criteria, sub-iteration procedure is initiated, step (2) is repeated and the next pseudo-time level becomes m + 1 (keeping only the new time metrics for the m+1 sub-iteration); otherwise, the flow field and movement of the body are obtained and step (2) is repeated to start the next new physical time step.

RESULTS

All the computations presented here were carried out for the following flow parameters: free stream Mach number $M_\infty = 0.2$, and Reynolds number $\text{Re}_D = 30,000$. A small disturbance was placed near the tip and its height in all cases was set to h/D=0.004 and its roll angle position to $\Phi = 90°$, i.e., perpendicular to windward plane of symmetry (for the moving body this was the initial angle). We describe the investigation of three angles of attack: $\alpha = 20°$, $\alpha = 40°$ and $\alpha = 65°$ which represent three typical regimes for the flow around pointed slender bodies of revolution.

$\alpha = 20°$

For the fixed configuration, i.e., the body is not allowed to rotate, the flow converged to a steady state with moment coefficient values for the rolling moment $C_{Mx} = 0.0001$, pitching moment $C_{My} = -8.0$ and yawing moment $C_{Mz} = -1.65$. If the disturbance is removed the flow becomes symmetric again and returns to its original undisturbed shape (convection instability). A typical snapshot of density contours cross plane at the ogive-forebody and the cylinder afterbody junction is shown in Fig. 2.
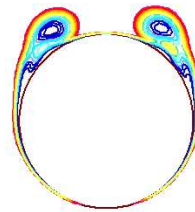
Figure 2. Density contours in cross section at x/D=3.5 for a fixed body; $\alpha = 20°$.

When the body is allowed to roll, the structural parameters were chosen by trial and error to allow large rolling amplitudes:

$$k_\phi = 1.0 \times 10^{-5}, \, d_\phi = 1.0 \times 10^{-8}, \mu = 2 \times 10^{-4}, \gamma = 0.0176.$$

The corresponding natural frequency and damping ratio for these conditions are $\omega_\phi \sim 0.024$ and $\xi_\phi \sim 0.000075$, respectively. For these values even the small initial rolling moment was sufficient to create a significant change in the flow-structure interaction that can be seen from the time histories of the moment coefficients and the roll angle of the body in Fig. 3. In contrast to the multi-frequency behavior of the moments acting on the body, the roll ϕ is almost harmonic oscillating with a period equal to the inverse of its resonance frequency $(f = \omega_\phi / 2\pi \sim 0.0038)$. However, note that the moment periodicity (i.e. its lowest frequency) is identical to that of the roll. It is evident that under the current set of parameter the body does not follow the roll moment that drives its 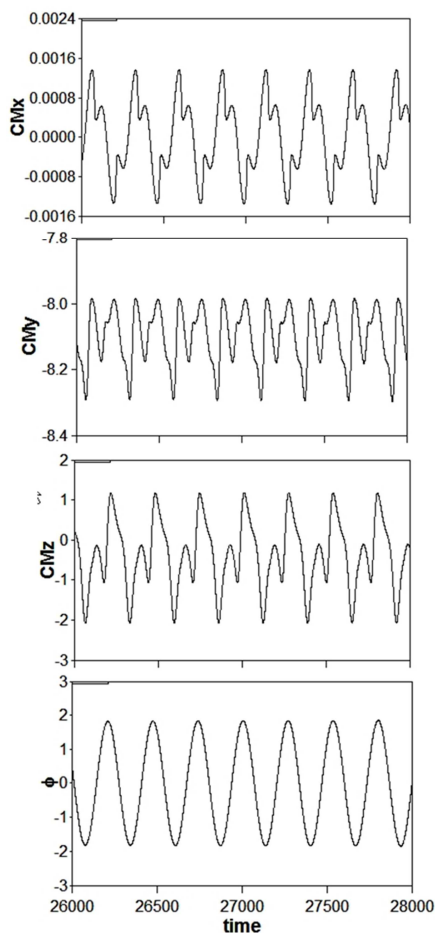motion. However, an increase in the damping ratio will be shown to regularize the multi-frequency moments resulting with a standard out-of-phase response for the roll and its generating moment.

$$\underline{\alpha = 40^\circ}$$

For the fixed configuration, i.e., the body is not allowed to rotate, the flow at this high angle of attack does not converge to a steady state as shown in Fig. 4, and rather oscillates harmonically with low amplitudes and the same frequency for all moments and with average values of moment coefficients of rolling moment $C_{Mx} = 0.00052$, pitching moment $C_{My} = -35.9$ and yawing moment $C_{Mz} = -4.1$. The oscillations are due to vortex shedding from the cylindrical afterbody. The shedding stops if a shorter 3.0-diam cylindrical afterbody is used. If the disturbance is removed the flow becomes symmetric again and oscillations ceased (convection instability). A snapshot of the density contours cross plane at the ogive-forebody and the cylinder afterbody junction is shown in Fig. 5, and demonstrates a large asymmetry of the flow. When the body is allowed to roll, the structural parameters were kept as in the previous case for $\alpha = 20^\circ$.
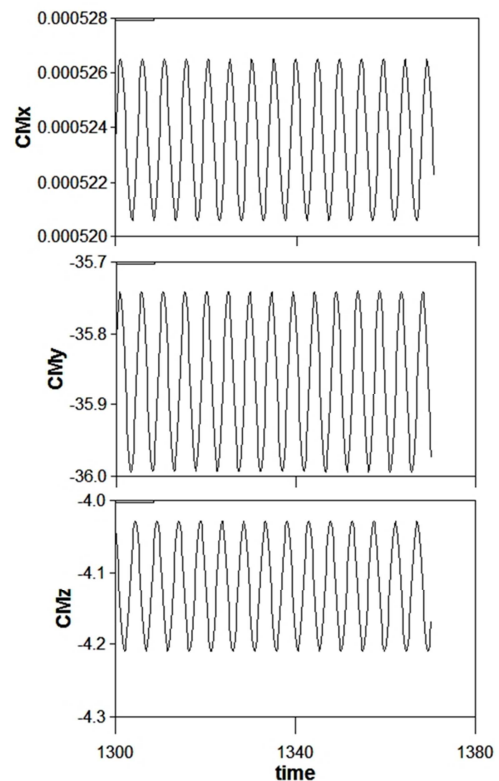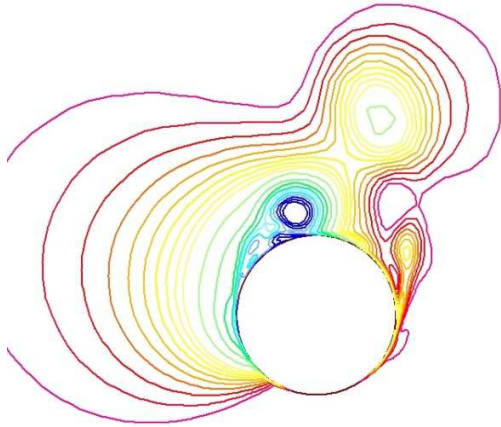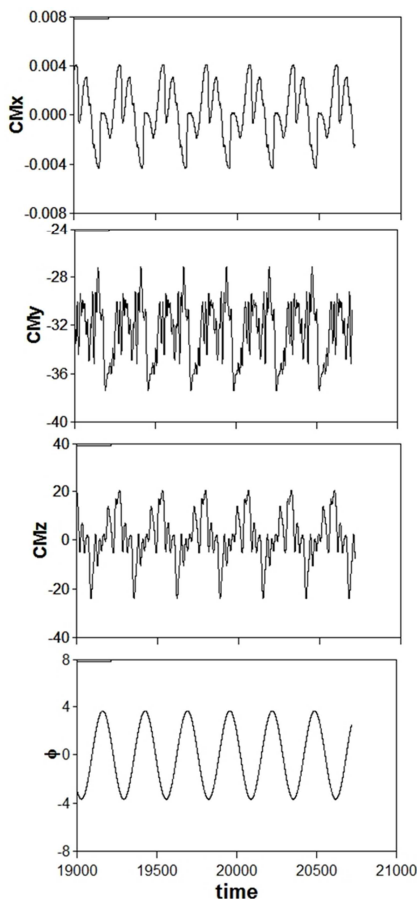

Figure 3. Time histories of moment coefficients and roll at angle of attack of $\alpha = 20^\circ$.

Figure 4. Time histories of moment coefficients for a fixed body at angle of attack of $\alpha = 40^\circ$.

Figure 5. Density contours in cross section at x/D=3.5 for a fixed body; $\alpha = 40^\circ$.

The time histories of the moment coefficients appear as large-amplitude mutli-frequency ultrasubharmonics with large amplitudes (Fig. 6) with the average values near those of the

fixed body. The roll angle amplitudes are very large $(A(\phi) = \pm 4)$, but as in the case of $\alpha = 20^\circ$, the roll ϕ is almost harmonic with a frequency close to the that of the structural resonance ($f = \omega_\phi / 2\pi \sim 0.0038$) which is identical to the lowest frequency of the moments.

$\alpha = 65^\circ$

Case I: $k_\phi = 1.0 \times 10^{-5}$, $d_\phi = 1.0 \times 10^{-8}$

For the fixed configuration the flow at this very high angle of attack does not converge to a steady state and resembles the non-stationary behavior of the flow around a long inclined cylinder, as shown in Fig. 7, with average values of moment coefficients of rolling moment $C_{Mx} = 0.0002$, pitching moment $C_{My} = -51.8$ and yawing moment $C_{Mz} = -3.0$. If the disturbance is removed, in contrast to the previous cases of the lower angles of attack, the flow does not return to its original undisturbed shape and oscillates with amplitudes of the same order of magnitude as those of the disturbed case or even larger but with the mean of C_{Mx} and C_{Mz} about zero (absolute instability).

Figure 6. Time histories of moment coefficients and roll at angle of attack of $\alpha = 40^\circ$.
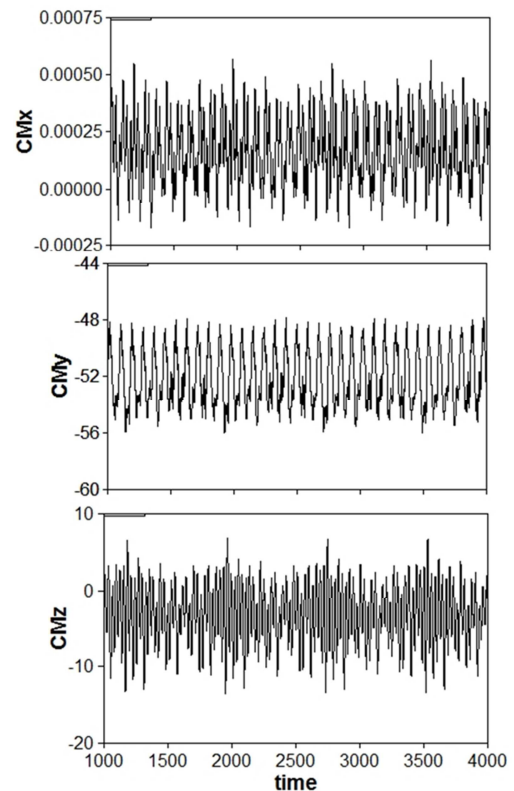
Figure 7. Time histories of moment coefficients for a fixed body at angle of attack of $\alpha = 65^\circ$.

A snapshot of the density contours cross plane at the ogive-forebody and the cylinder afterbody junction is shown in Fig. 8, appears like classical vortex shedding. When the body is allowed to roll, with the same structural parameters as in the previous cases for $\alpha = 20^\circ$ and $\alpha = 40^\circ$, the time histories of the moment coefficients appear also as large-amplitude mutli-frequency ultrasubharmonics (Fig. 9) but are significantly different than the corresponding moments of the fixed body (Fig. 7). The average values are closed to those of the fixed body, but amplitudes are much larger especially for the rolling and the yawing moments. The roll angle amplitudes are even larger than those of the case of $\alpha = 40^\circ$ ($A(\phi) = \pm 5$), but as in the previous cases of $\alpha = 20^\circ$ and $\alpha = 40^\circ$, the roll ϕ is harmonic with the structural resonance frequency $(f = \omega_\phi / 2\pi \sim 0.0038)$ which is identical to the lowest frequency of the moments.

Figure 9. Time histories of moment coefficients and roll at angle of attack of $\alpha = 65^\circ$.

Figure 8. Density contours in cross section at x/D=3.5 for a fixed body; $\alpha = 65^\circ$.

Case II: $k_\phi = 1.0 \times 10^{-2}$, $d_\phi = 1.0 \times 10^{-2}$

Increasing the spring stiffness and damping parameters of the structure reduce the roll amplitude significantly $(A(\phi) = \pm 0.03)$ even for an angle-of-attack of $\alpha = 65^\circ$ and the same with the amplitude of yawing-moment and pitching-moment coefficients while the amplitude of the rolling-moment coefficient is an order of magnitude larger (Fig. 10). But the most significant change is the fact that the roll angle ϕ becomes distinctly quasiperiodic and follows the rolling moment (with a time lag), in contrast to the results of Case I.

314
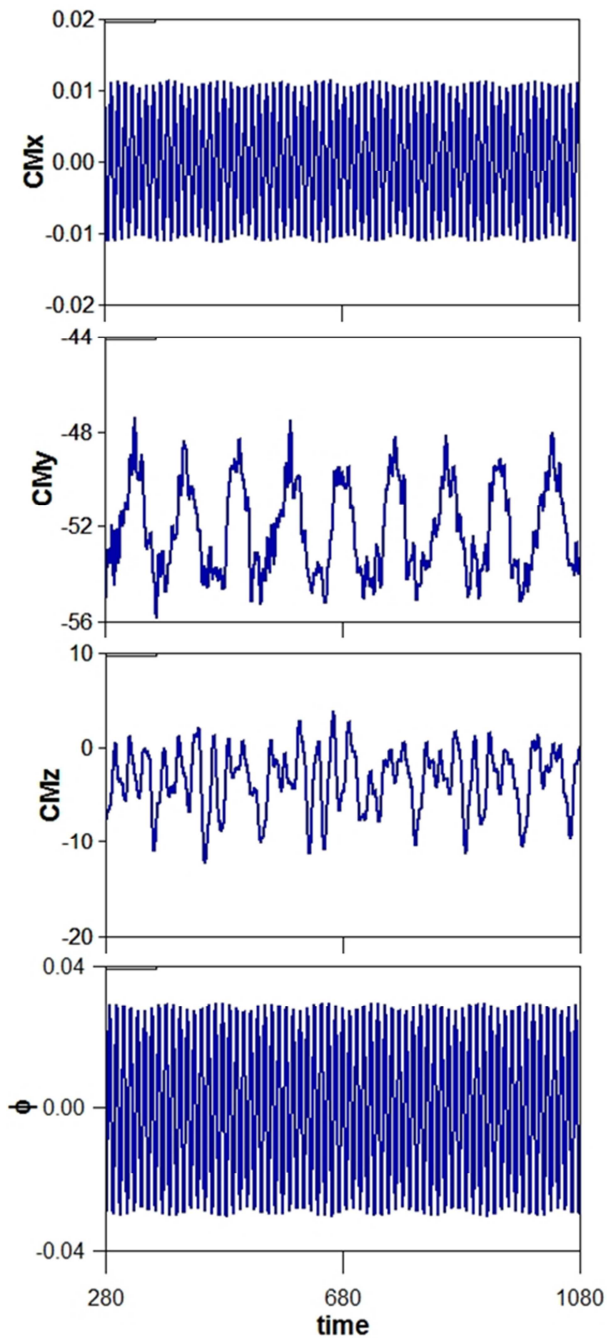
Figure 10. **Time histories of moment coefficients and roll with structure parameters** $k_\phi = 1.0 \times 10^{-2}$, $d_\phi = 1.0 \times 10^{-2}$ **at angle of attack of** $\alpha = 65^\circ$.

When the disturbance is removed and the computation is continued with the above solution as initial conditions, the yawing moment becomes symmetric and with a much small amplitude. However, the roll angle becomes smaller but it keeps the same form and frequencies (Fig. 11).
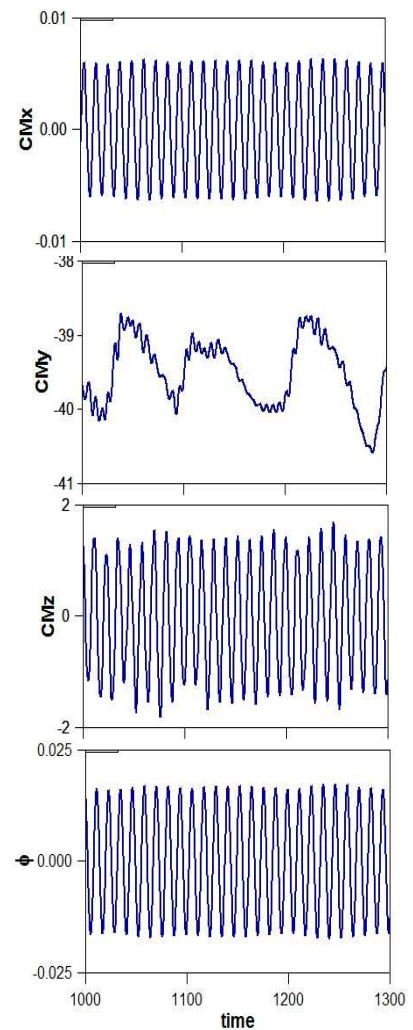
Figure 11. **Time histories of moment coefficients and roll with structure parameters** $k_\phi = 1.0 \times 10^{-2}$, $d_\phi = 1.0 \times 10^{-2}$ **when disturbance is removed. Angle of attack** $\alpha = 65^\circ$.

CLOSING REMARKS

We conduct a numerical investigation of the flow around an inclined tangent ogive-cylindrical body, placed in a wind tunnel at a high angle of attack and allowed to rotate around its longitudinal axis of symmetry. The body is subjected to three-dimensional, compressible, laminar flow at Reynolds number of 30,000 based on the body diameter and a Mach number of 0.2. A second-order implicit finite difference scheme is employed for the flow equations, adapted to three-dimensional curvilinear coordinate system, whereas the coupled structural equation is solved by an explicit fourth-order Runge-Kutta method.

We describe the investigation of three angles of attack $\alpha = 20^\circ$, $\alpha = 40^\circ$ and $\alpha = 65^\circ$ both for fixed and free-to-roll configurations. For each angle of attack the free-to-roll

configuration portrays a distinct and different behavior pattern. Depending on structure characteristics and flow conditions even a small rolling moment coefficient may lead to large amplitude roll oscillations.

A direct implication of this investigation is that roll moments due to viscous effects of vortex asymmetry and unsteadiness can have significant effects when pointed slender bodies of revolution are subjected to flows with varying angles of attack. This should be taken into account when stability or maneuverability of such bodies is considered.

REFERENCES

[1] Lamont, P.J. and Hunt, B.L., "Pressure and Force Distributions on a Sharp-Nosed Circular Cylinder at Large Angles of Inclination to a Uniform, Subsonic Stream," *Journal of Fluid Mechanics,* Vol. 76, Pt. 3, 1976, pp. 519-559.

[2] Degani, D. and Tobak, M., "Effect of Upstream Disturbance on Flow Asymmetry." AIAA Aerospace Sciences Meeting, Reno, Nevada, January 1992. AIAA paper 92-0408.

[3] Dexter, P. C., and Hunt, B. L., "The Effects of Roll Angle on the Flow over a Slender Body of Revolution at High Angle of Attack," AIAA Paper 81-0358, Jan. 1981.

[4] Degani, D., "Effect of Geometrical Disturbance on Vortex Asymmetry." *AIAA Journal*, 1991, Vol. 29, No. 5, pp. 560-566.

[5] Zilliac, G.G., Degani, D. and Tobak, M., "Asymmetric Vortices on a Slender Body of Revolution." *AIAA Journal*, 1991, Vol. 29, No. 4, pp. 667-675.

[6] Moskovitz, C. A., Hall, R. M., and DeJarnette, F. R., "Effects of Nose Bluntness, Roughness and Surface Perturbations on the Asymmetric Flow Past Slender Bodies at Large Angles of Attack,"AIAA Paper 88-2236CP, Aug. 1989.

[7] Degani, D. and Tobak, M.: "Experimental study of controlled tip disturbance effect on flow asymmetry," *Physics of Fluids A*, 1992, Vol. 4, No. 12, pp. 2825-2832.

[8] Brandon, J. M. and Nguyen, L. T., "Experimental Study of Effects of Forebody Geometry on High Angle of Attack Stability," *Journal of Aircraft,* Vol. 25, July 1988, pp. 591-597.

[9] Deane, J. R., "Experimental Investigation into the Interaction Between Body Vortices and Wing Panels on a Missile Configuration at Low Speed," AIAA Paper 80-0032, Jan. 1980.

[10] Ericsson, L. E., "Wing Rock Generated by Forebody Vortices," *Journal of Aircraft,* Vol. 26, Feb. 1989, pp. 110-116.

[11] Ericsson, L. E., "A Possible Causative Flow Mechanism for Body Rock," *Journal of Aircraft,* Vol. 22, May 1985, pp. 441-443.

[12] Keener, E. R., Chapman, G. T., Cohen, L., and Teleghani, J., "Side Forces on Forebodies at High Angles of Attack at Mach Numbers from 0.1 to 0.7. Two Tangent Ogives, Paraboloid and Cone," NASA TMX-3438, Feb. 1977.

[13] Yoshinaga, T., Tate, A., and Inoue, K., "Coning Motion of Slender Bodies at High Angles of Attack in Low Speed Flow," AIAA Paper 81-2485, Aug. 1981.

[14] Wang, B., Deng, X. Y., Ma, B.F., and Rong, Z., "Effect of tip perturbation and wing locations on rolling oscillation induced by forebody vortices," *Acta Mech Sin,* 26, 2010, pp.787-791.

[15] Pulliam, T.H. and Steger, J. L., "Implicit Finite-Difference Simulations of Three-Dimensional Compressible Flow,*"* *AIAA Journal*, Vol. 18, No.2, 1980, pp. 159-167

[16] Beam, R. M. and Warming, R. F., "An Implicit Factored Scheme for Compressible Navier-Stokes Equations," *AIAA Journal*, Vol. 16, No. 6, 1978, pp. 393-402

[17] Steger, J. L., "Implicit Finite-Difference Simulation of Flow About Arbitrary Two-Dimensional Geometries,*"AIAA Journal,* Vol. 16, No. 7, 1978, pp. 679-686

[18] Degani,D. and Marcus, S.W., "Thin vs Full Navier-Stokes Computation for High-Angle-of-Attack Aerodynamics," *AIAA Journal*, Vol. 35, No. 3, 1997, pp. 565-567

[19] Meirovitch, L., Methods of Analytical Dynamics, Wiley, 1988.
[20] Gendel, S., Gottlieb, O. and Degani, D., "Fluid-Structure Interaction of an Elastically Mounted Slender Body at High Incidence," *AIAA Journal*, 2014. doi: 10.2514/1.J053416
[21] Blades, E. L., and Newman , J. C., "Aeroelastic Effects of Spinning Missiles," 48th AIAA/ASME/ASCE/ AHS/ASC Structures, Structural Dynamics, and Materials Conference, April 2007, Honolulu, Hawaii. AIAA Paper 2007-2243
[22] Chen X.-Y., Zha G.-C., "Fully coupled fluid-structural interactions using an efficient high resolution upwind scheme," Journal of Fluids and Structures, Vol. 20, 2005, pp. 1105-1125

Critical Anomaly Effects in Trans-Critical Fluid Flows in Capillaries

B. Zappoli[1,*], J. Ouazzani[2], C. Lecoutre[3,4], S. Marre[3,4], S. Morais[3,4], R. Guillaument[3,4], Y. Garrabos[3,4]

[1] *CNES, Avenue Edouard Belin 18, F-31401 Toulouse Cedex 9, France*
[2] *ARCOFLUID, 3 rue du Golf, F-33701 Mérignac Cedex, France*
[3] *CNRS, ICMCB ESEME, UPR 9048, F-33600 Pessac Cedex, France*
[4] *Univ. Bordeaux, ICMCB, UPR 9048, F-33600 Pessac Cedex, France and*
*Author for correspondence: CNES, 18 Avenue Edouard Belin,
F-31401 Toulouse Cedex 9, France. E-mail: zappoli.bernard@free.fr

The thermal and dynamical properties of steady state, near-critical fluid flows in capillaries are explored by the numerical analysis of the Navier-Stokes equations written for a Newtonian, heat conducting and viscous van der Waals fluid. We focus on how the different critical transport coefficients anomalies dominate the fluid flow in a capillary duct of constant section. This configuration is of great interest for cooling technologies, cryogen-tightness in launchers technologies. The perturbation of the basic, isothermal flow associated to the radial heat conduction is studied numerically and confirms the existence of three zones where different mechanisms prevail. The first zone extends from the capillary inlet to the critical cross section. In a narrow layer surrounding the critical cross section, the effects of the diverging fluid properties becomes prominent and manifest thermo-mechanical coupling mechanisms on the flow. The heat transfer brought in by the longitudinal, forced convection compensates the diverging temperature drop. In the third zone, the temperature increases again to reach the wall temperature. By implementing simplified or more realistic models of the thermal conductivity singular behavior, our numerical results are consistent with the previous asymptotic analysis for hydrogen case and confirm the significant temperature drop in the critical cross section for carbon dioxide case.

Latin		Greek	
a, b	van der Waals parameters of the fluid	μ, η_b	dynamic (shear) and bulk viscosity
c_p, c_V	specific heat at constant pressure and volume	κ_T	isothermal compressibility
F	non dimensional functions	ρ	density
k_B	Boltzmann constant	χ_T^*	scaled isothermal susceptibility
L, R	length and internal radius of the tube	Subscripts	
M	molar mass of the fluid	as	asymptotic
p	pressure	c	critical parameter
Pr	Prandtl number	co	crossover
Q	mass flow	e	density excess
Re_R	Reynolds number based on the tube radius	IG	Ideal-gas parameter
T	temperature	IN	inlet
V	volume	OUT	outlet
$r = \frac{R_{\mathrm{IG}}}{M}$	Ideal-gas constant of the fluid	MF	mean-field
R_{IG}	Ideal gas molar constant	p, ρ, V	constant pressure, density, volume
u, v	longitudinal and radial velocity components	vdW	van der Waals
z, r	longitudinal and radial coordinates	z, r	first-order derivative with respect to z, r
Greek		zz, rr	second-order derivative with respect to z, r
β, γ, ν	universal critical exponents	0	first-order solution
β_p	isobaric expansion coefficient	00	zero-density limit
$\epsilon = \frac{R}{L}$	aspect ratio	Decorated	
λ	thermal conductivity coefficient	$^-$	regular or particular scaled quantity
$\Delta\lambda$	critical enhancement of λ		

Table I: Nomenclature

I. INTRODUCTION

Due to short-ranged attractive forces between the particles, high pressure and high density fluids exhibit a critical point in their phase diagram where the thermodynamics and transport properties show power law anomalies [1, 2]. At critical density, the

isothermal compressibility, the isothermal expansion coefficient, the heat capacities at constant pressure or constant volume, and the heat conductivity, tend to infinity when the temperature approaches the critical conditions while the power laws are such that the heat diffusion coefficient tends to zero. However, in such near critical conditions, fluids are continuous media that can be described by the Navier-Stokes equations provided the transport coefficients account for the above-mentioned anomalous behaviors [3]. Beyond fundamental statistical physics questions, one-phase (supercritical), near critical fluids thus also address macroscopic hydrodynamics problems that have been extensively studied [4]. In the present work, we address pressure-driven forced convection of transcritical fluids in capillaries, which belong to a new significant class of thermomechanical coupling problems. Indeed, this work comes after the initial approach given in Ref. [5] from the asymptotic analysis of this type of flow. Such a preliminary work has reaveled interesting second-order contributions of the thermal effects through the capillary wall, with noticeable consequences for engineering small scale investigations of leakage, infiltration path, etc. We basically keep the same configuration, but we analyze numerically the structure of the fluid flows that go through the critical point in the capillaries with large departures from the critical conditions. We solve the van der Waals fluid equations of motion. We identify the different regions where the different critical anomalies prevail. We focus our result presentation on the thermal effects. We compare with the previously obtained asymptotic solutions for hydrogen to confirm the validity of the numerical code, and compute the solution for carbon dioxide in the challenging perspective of designing an experiment for validation.

II. THE MODEL AND THE GOVERNING EQUATIONS

A. The model

We consider a steady state, van der Waals fluid flow in a cylindrical microchannel that joins two (infinite in thermal conductivity and in size) reservoirs, both being then maintained at constant temperature $T = T_c$ and at constant, different inlet p_{IN} and outlet p_{OUT} pressures (Fig. 1), with $p_{IN} > p_c$ and $p_{OUT} < p_c$, respectively (i.e., at constant, different inlet $\rho_{IN} > \rho_c$ and outlet $\rho_{OUT} < \rho_c$ densities, consequently). The channel wall is maintained at $T = T_c$. The channel sizes are $2R = 20\,\mu m$ in diameter and $L = 30\,cm$ in length, leading to a small value of the aspect ratio $\varepsilon = \frac{R}{L} = 3.33 \times 10^{-5} \ll 1$.

In practical situations, the channel can be tortuous and the wall temperature may differ from the critical temperature because of the finite heat conductivity of
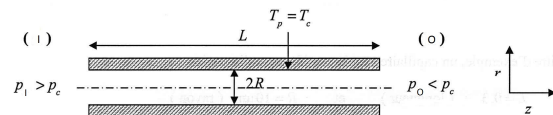

Figure 1: The model: a 2-D, cylindrically symmetric, capillary tube of $2R = 20\,\mu m$ in diameter and $L = 30\,cm$ in length joins two reservoirs at different pressures, higher and lower than the critical pressure, respectively. The capillary wall, of small aspect ratio $\varepsilon = \frac{R}{L} = 3.33 \times 10^{-5} \ll 1$, is maintained at the critical temperature.

the wall. However, as the inlet and outlet pressures are higher and lower than the critical pressure, respectively, the critical pressure is reached in a section of the channel where $T \sim T_c$. We can anticipate on the analysis by noting that in our ideal cylindrical tube of constant wall temperature $T = T_c$ over the finite length $L \gg R$, the fluid temperature is initially homogeneous and equal to T_c. The fluid reaches thus the critical state conditions in some location within the capillary. This particular configuration has been chosen to highlight the critical anomalies effects. The fluid is considered to be steady laminar, Newtonian, compressible, viscous and heat conducting [4, 6, 7]. In the steady state, the local thermodynamic fluid properties and the velocity are given by the well-known, mass, momentum and enthalpy balance equations (see Ref. [4] for their detailed notations and derivations) where the times derivatives are set to zero. The flow field, where u and v are the longitudinal and radial velocity components, is supposed to be cylindrically axisymmetric in the longitudinal z-axis and the radial r-axis of the coordinates, so that the derivatives with respect to the azimuthal angle θ have been dropped in the governing equations. Moreover, as the critical density is large, the fluid is a continuous media and the no slip condition is considered for the velocity on the capillary walls. The pressure is homogeneous in the inlet and outlet planes. For symmetry reasons the velocity components, their gradients as well as the temperature gradient are zero along the z axis. For simplicity on the present analysis, we finally note that only the non-dimensional forms of the governing equations will be written when needed later on.

These equations are closed by the van der Waals equation of state

$$p = \frac{\rho r T}{1 - b\rho} - a\rho^2 \qquad (1)$$

where $a = \frac{3p_{c,vdW}}{\rho_c^2}$ and $b = \frac{1}{3\rho_c}$ are the van der Waals parameters of the fluid, selecting the experimental values of T_c and ρ_c as entry data to characterize the fluid. $r = \frac{R_{IG}}{M} = \frac{8p_{c,vdW}}{3\rho_c T_c}$ (not to be confused with the radial r-coordinate) is the ideal gas constant of the fluid that defines the van der Waals critical pressure

$p_{c,\mathrm{vdw}}$. Indeed, the value of $p_{c,\mathrm{vdw}}$ differs from experimental value of p_c due to the difference between the fluid critical compressibility factor $Z_c = \frac{p_c}{\rho_c r T_c}$ and the van der Waals critical compressibility factor $Z_{c,\mathrm{vdw}} = \frac{3}{8} = \frac{p_{c,\mathrm{vdw}}}{\rho_c r T_c}$. The van der Waals equation of state, so-called the mean-field approximation of the fluid equation of state (i.e., when the true contribution of the critical fluctuations is approximated), while non-exact to describe the singular behavior of Ising-like critical systems very close to the critical point, often proved to give satisfactory phenomenological approach of the thermomechanical coupling phenomena in real fluids [4–6]. The isobaric expansion coefficient β_p the inverse isothermal compressibility $(\kappa_T)^{-1}$, and the specific heat at constant pressure c_p, only depend on Eq. 1, and can be written as follows:

$$
\begin{aligned}
\beta_p &= -\frac{1}{\rho}\left(\frac{\partial \rho}{\partial T}\right)_p = \frac{\rho r}{p - a(1 - 2b\rho)\rho^2} \\
(\kappa_T)^{-1} &= \rho\left(\frac{\partial p}{\partial \rho}\right)_T = \frac{\rho r T}{(1 - b\rho)^2} - 2a\rho^2 \\
c_p &= c_{V\mathrm{IG}} - \frac{rT}{1 - b\rho}\beta_p \\
c_p &= c_{V\mathrm{IG}} + \frac{\rho r^2 T}{(1 - b\rho)^2}\kappa_T
\end{aligned}
\tag{2}
$$

where $c_{V\mathrm{IG}}$ is the heat capacity at constant volume for the ideal gas (here, $c_{V\mathrm{IG}} = \frac{5}{2}r$ for hydrogen and carbon dioxide cases). It should be mentioned that $\beta_p \sim \kappa_T \sim (\rho - \rho_c)^{-2}$ along the critical isotherm.

The model must be complemented by a statistical mechanics input for the dynamical (shear) viscosity μ and the heat conductivity λ coefficients [8], which also belong to the above mean field approximation. For the viscosity case, μ shows a small power law exponent near the critical point [8] and can be considered as an ideal-gas-like (or mean field) constant property in our modelling [4]. Therefore $\mu = \mu_{\mathrm{IG}}$, where μ_{IG} is the shear viscosity for the ideal-gas at a selected convenient temperature, and the viscous effects can be accounted for using the Navier-Stokes assumption $\frac{2}{3}\mu + \eta_b = 0$. For the heat conductivity case, we consider two different expressions. The first one, referred to as λ-model 1, similar to the one used in [5], is a simplified expression that shows an asymptotic behavior of λ that is depending on $(T - T_c)^{-\frac{1}{2}}$ and $(\rho - \rho_c)^{-\frac{1}{2}}$ when approaching the critical point along the critical isochore and the critical isotherm, respectively. For such power law dependences, λ-model 1 can be written as follows.

$$
\lambda = \lambda_{\mathrm{IG}}\left[\Lambda_1 \frac{T - T_c}{\frac{p_{c,\mathrm{vdW}}}{\frac{3}{8}\rho_c r}} + \Lambda_2 \frac{\rho - \rho_c}{\rho_c}\right]^{-\frac{1}{2}}
\tag{3}
$$

where λ_{IG} is the thermal conductivity for the ideal-gas and Λ_1 and Λ_2 are non-dimensional constants of order one. In this equation the asymptotic temperature behavior on the critical isochore agree with the one expected from the mean-field approximation while it is only a simple, but arbitrary, functional density

behavior along the critical isotherm. Its simple form using $\Lambda_1 = \Lambda_2 = 1$ made an asymptotic analysis possible [5] but is therefore physically invalid, even if, as will be shown, the results are not so far from that given by our present more realistic numerical analysis reported below. Indeed, the corresponding analytical asymptotic solution that was obtained in [5] will be here checked by comparison with the numerical solution obtained below using our numerical method with the same λ-model 1 for the thermal conductivity.

The second expression, referred to as λ-model 2, is a more complete expression for λ including three distinct contribution terms, as analyzed in [8]:

$$
\lambda(T, \rho, \Delta T, \Delta\rho) = \lambda_{00}(T) + \lambda_e(\rho) + \Delta\lambda(|\Delta T|, |\Delta\rho|)
\tag{4}
$$

$\lambda_{00}(T)$ is the thermal conductivity in the limit of zero-density, therefore only temperature dependent. $\lambda_e(\rho)$ is commonly referred to in the engineering literature as the density-excess of the thermal conductivity and then assumed only density-dependent. Generally, $\lambda_{00}(T) + \lambda_e(\rho) = \bar{\lambda}(T, \rho)$ is referred to as the regular thermal conductivity, which can be used to calculate the thermal conductivity far from the critical point. Obviously, $\Delta\lambda(|\Delta T|, |\Delta\rho|)$ is the critical enhancement of the thermal conductivity that accounts for the singular behavior of λ in the critical region. Unfortunately, such a complete expression is not in a convenient functional form to make an asymptotic analysis possible and, moreover, the fluid parameters involved in Eq. 4 are little known for hydrogen. Therefore, we have used this λ-model 2 only for the numerical modelling of CO_2, for which these three distinct contribution terms can be written as follows,

$$
\lambda_{00}(\bar{T}) = \frac{(\bar{T})^{-\frac{1}{2}}}{\sum\limits_{k=0}^{k=3} a_k (\bar{T})^{-k}}
\tag{5}
$$

with $a_0 = 32.3537$, $a_1 = 77.1034$, $a_2 = 618.115$, $a_3 = -613.848$, expressed in $\mathrm{W}^{-1}\mathrm{mK}$.

$$
\lambda_e(\bar{\rho}) = \sum\limits_{k=1}^{k=3} b_k (\bar{\rho})^k
\tag{6}
$$

with $b_1 = 0.33789 \times 10^{-2}$, $b_2 = 0.27725 \times 10^{-3}$, $b_3 = 0.47396 \times 10^{-4}$, expressed in $\mathrm{Wm}^{-1}\mathrm{K}^{-1}$. In the above Eqs. 5 and 6, we note that are introduced the practical non-dimensional variables $\bar{T} = \frac{T}{T_{r,\mathrm{CO}_2}}$ and $\bar{\rho} = \frac{\rho}{\rho_{r,\mathrm{CO}_2}}$, where $T_{r,\mathrm{CO}_2} = 100\,\mathrm{K}$ and $\rho_{r,\mathrm{CO}_2} = 100\,\mathrm{kgm}^{-3}$.

$\Delta\lambda$ can be obtained from the Stokes-Einstein diffusion coefficient, introducing then a non-dimensional crossover function $F_{\mathrm{co}}(|\Delta T|, |\Delta\rho|)$, which accounts

for the singular behavior on $|\Delta T| = \left| \frac{T}{T_c} - 1 \right|$ and $|\Delta \rho| = \left| \frac{\rho}{\rho_c} - 1 \right|$ when approaching the critical point, and which provides the expected decrease to zero value of $\Delta \lambda$ far from the critical point. In addition, the calculation of the diffusion coefficient needs to introduce also $\frac{T_c}{p_c} \left(\frac{\partial p}{\partial T} \right)_\rho = \frac{8 \frac{\rho}{\rho_c}}{3 - \frac{\rho}{\rho_c}}$ (obtained from Eq. 1) and to use the mean-field relation $\xi = \xi_{0\mathrm{MF}} \left(\frac{\chi_{T\mathrm{vdW}}^*}{\Gamma_{\mathrm{vdW}}} \right)^{\frac{1}{2}}$ between the correlation length ξ and the non-dimensional isothermal susceptibility $\chi_T^* = \left(\frac{\rho}{\rho_c} \right)^2 p_{c\mathrm{vdW}} \kappa_T$, where $\kappa_T = \frac{1}{\rho} \left(\frac{\partial \rho}{\partial p} \right)_T$ is the isothermal compressibility (see Eq. 2). We note that the mean-field amplitudes $\xi_{0\mathrm{MF}}$ and Γ_{vdW} comes from the mean-field singular behaviors $\xi = \xi_{0\mathrm{MF}} (\Delta T)^{-\frac{1}{2}}$ and $\chi_T^* = \Gamma_{\mathrm{vdW}} (\Delta T)^{-1}$ in the homogeneous domain along the critical isochore ($\Delta \rho = 0$). χ_T^* only depends on Eq. 1, and can be written as follows:

$$\chi_T^* = \frac{\frac{\rho}{\rho_c} \left(3 - \frac{\rho}{\rho_c} \right)^2}{24 \frac{T}{T_c} - 6 \frac{\rho}{\rho_c} \left(3 - \frac{\rho}{\rho_c} \right)^2} \qquad (7)$$

As a result, $\Delta \lambda$ writes such as [8]

$$\Delta \lambda = \frac{k_B p_{c\mathrm{vdW}}}{\mu_{\mathrm{MF}} \xi_{0\mathrm{MF}}} \frac{\Lambda}{6\pi} (\Gamma_{\mathrm{vdW}})^{\frac{1}{2}} F_{\mathrm{vdW}} F_{\mathrm{co}} \qquad (8)$$

where the prefactor ratio $\frac{k_B p_{c,\mathrm{vdW}}}{\mu_{\mathrm{MF}} \xi_{0\mathrm{MF}}}$ only involves dimensioned quantities, in particular the regular (i.e., constant) shear viscosity μ_{MF} of a van der Waals fluid at the critical point [4]. The ratio $\frac{\Lambda}{6\pi}$ appears in the diffusion coefficient calculated from the renormalization group theory. In Eq. 8, the non-dimensional functions F_{vdW} and F_{co} write as follows

$$F_{\mathrm{vdW}} = \left(\frac{T}{T_c} \frac{\rho_c}{\rho} \right)^2 \left[\frac{8 \frac{\rho}{\rho_c}}{3 - \frac{\rho}{\rho_c}} \right]^2 \left[\frac{\frac{\rho}{\rho_c} \left(3 - \frac{\rho}{\rho_c} \right)^2}{24 \frac{T}{T_c} - 6 \frac{\rho}{\rho_c} \left(3 - \frac{\rho}{\rho_c} \right)^2} \right]^{\frac{1}{2}} \quad (a)$$

$$F_{\mathrm{co}} = \left(\frac{\rho}{\rho_c} \right)^n \exp \left[-A_\lambda (|\Delta T|)^2 - B_\lambda (|\Delta \rho|)^4 \right] \quad (b)$$
$$(9)$$

with F_{vdW} only depending on the van der Waals Eq. 1. All the needed values of the constants and fluid parameters involved in Eqs. 8 and 9 are given in Table II, with $n = 0$ in the above crossover function. Unlike in most of the fundamental researches cited here, we note that the dependence in density is considered to account for large (non perturbative) departures from the critical density.

B. The non dimensional equations

We choose L, R as the length scales in the longitudinal z-direction and in the radial r-direction, respectively, and ρ_c, $p_{c,\mathrm{vdW}}$, as density and pressure

		H$_2$	CO$_2$
k_B (JK^{-1})	1.38×10^{-23}		
r (Jkg^{-1}K^{-1})		4.12×10^3	0.189×10^3
a (m^{3}kg^{-1}K)		51.146	138.18
b (10^{-5}m^{3}kg^{-1})		110.71	71.255
$c_{p\mathrm{IG}}$ (Jkg^{-1}K^{-1})		1.442×10^4	0.662×10^3
$\gamma_{\mathrm{IG}} = \frac{c_{Vp\mathrm{IG}}}{c_{p\mathrm{IG}}}$	1.4		
p_{IN}/p_c		1.5	1.05
p_{OUT}/p_c		0.8	0.95
T_c (K))		32.938	304.14
ρ_c (kgm^{-3})		31.36	467.8
$p_{c,\mathrm{vdW}}$ (MPa)		1.546	10.08
μ_{IG} (Pas)		8.9×10^{-6}	14.7×10^{-6}
λ_{IG} (Wm^{-1}K^{-1})		0.176	0.016
Pr$_{\mathrm{IG}}$		1.59×10^{-2}	0.732
εRe$_R$		0.0168	0.474
Λ	1.02		
Γ_{vdW}	$\frac{1}{6}$		
μ_{vdW} (Pas)			32.7×10^{-6}
$\xi_{0\mathrm{MF}}$ (m)			1.5×10^{-10}
A_λ			$39, 8$
B_λ			$5, 45$

Table II: Fluid parameters

scales, respectively. The scale for the temperature corresponds to the temperature $T_{r,\mathrm{IG}}$ of an ideal-gas set at ρ_c and $p_{c,\mathrm{vdW}}$, e.g., $T_{r,\mathrm{IG}} = \frac{p_{c,\mathrm{vdW}}}{\rho_c r}$. One should note immediatly that the critical temperature in scaled variable is thus $\frac{T_c}{T_{r,\mathrm{IG}}} = \frac{8}{3}$, while the scale for the isobaric expansion coefficient is $\frac{1}{T_{r,\mathrm{IG}}} = \frac{\rho_c r}{p_{c,\mathrm{vdW}}}$. As the flow along the longitudinal axis of the capillary tube is driven by $p_{\mathrm{IN}} - p_{\mathrm{OUT}}$, the longitudinal and radial velocity scales are the Poiseuille velocity $U = \frac{p_c R^2}{4 \mu_{\mathrm{IG}} L}$ in the z-direction and the product εU in the r-direction, respectively, where we recall that the aspect-ratio $\varepsilon = \frac{R}{L} \ll 1$ is a small parameter due to our capillary geometry. Obviously, the natural scales for the specific heats, the viscosity and the thermal conductivity are $c_{p\mathrm{IG}}$ (with here $c_{p\mathrm{IG}} = \frac{7}{2}$, i.e., $\gamma_{\mathrm{IG}} = \frac{c_{p\mathrm{IG}}}{c_{V\mathrm{IG}}} = 1.4$), μ_{IG}, and λ_{IG}, respectively. By carrying the above definition of the scaling into the Navier Stokes equations, the basic non-dimensional governing equations write in similar reduced forms to the ones of Ref. [5], recovering the specific heat ratio γ_{IG}, the Prandtl number Pr$_{\mathrm{IG}} = \frac{\mu_{\mathrm{IG}} c_{p\mathrm{IG}}}{\lambda_{\mathrm{IG}}}$, the Reynolds number Re$_R = \frac{\rho_c U R}{\mu_{\mathrm{IG}}}$ and the product εRe$_R = \frac{\rho_c U R^2}{\mu_{\mathrm{IG}} L}$, where the latter one gives the relative magnitude of the inertia and viscous stresses for the longitudinal and radial motions, respectively. For the hydrogen

case, μ_{IG} and λ_{IG} are calculated from the kinetic gas theory at $T = 300\,K$, while their estimations for carbon dioxide case are discussed below. We note our subscript notation exchange from 0 in Ref. [5] to IG in present work, which avoids a confuse meaning in the ideal-gas origin of our reference scales when writing the first-order solution (see below Eqs. 10 with subscript 0) of the Navier-Stokes equations. Accordingly, the non dimensional forms of the thermodynamic and the transport (λ-model 1) properties are

$$p = \frac{3\rho T}{3-\rho} - 3\rho^2$$
$$\beta_p = \frac{\rho}{p - \rho^2(3-2\rho)}$$
$$c_p = \frac{1}{\gamma_{\mathrm{IG}}}\left[1 - \frac{3(\gamma_{\mathrm{IG}}-1)}{3-\rho}\beta_p\right]$$
$$\mu = 1$$
$$\lambda = \left[\Lambda_1\left(T - \frac{8}{3}\right) + \Lambda_2\left(\rho - 1\right)\right]^{-\frac{1}{2}}$$

where we note that the use of similar notation for the non-dimensional quantities is not confusing due to their association to the numerical values of the constants and amplitudes involved in the equations.

Now using the Taylor expansions close to the critical point of the properties involved in Eqs. 7, 8, and 9 for the λ-model 2 case, the non-dimensional asymptotical forms $(\chi_T^*)_{\mathrm{as}}^{-1}$ and $\Delta\lambda_{\mathrm{as}}$ of the $(\chi_T^*)^{-1}$ and $\Delta\lambda$ mean-field behaviors are

$$(\chi_T^*)_{\mathrm{as}}^{-1} = \frac{1}{\rho}\left[\Gamma_{\mathrm{vdW}}\left(T - \frac{8}{3}\right) - \frac{9}{2}\left(\rho - 1\right)^2 + .\right]$$
$$\Delta\lambda_{as} = \Lambda_{\mathrm{MF}}\left[\frac{9T}{8(3-\rho)}\right]^2\left[\frac{\rho\Gamma_{\mathrm{vdW}}}{(T-\frac{8}{3})-\frac{3}{4}(\rho-1)^2+.}\right]^{\frac{1}{2}}F_{\mathrm{co}}$$
$$F_{\mathrm{co}} = \exp\left[-A_\lambda\left(T - \frac{8}{3}\right)^2 - B_\lambda\left(\rho - 1\right)^4\right]$$
$$\text{with}\quad \Lambda_{\mathrm{MF}} = \frac{\Lambda}{6\pi}\frac{k_B p_{\mathrm{cvdW}}(\Gamma_{\mathrm{vdW}})^{\frac{1}{2}}}{\lambda_{\mathrm{IG}}\mu_{\mathrm{MF}}\xi_{0\mathrm{MF}}}$$

$\Delta\lambda_{as}$ shows the correct mean-field behavior of λ that is depending on $(T - T_c)^{-\frac{1}{2}}$ and $(\rho - \rho_c)^{-1}$ when approaching the critical point along the critical isochore and the critical isotherm, respectively.

The boundary conditions and symmetry properties that apply to the non dimensional variables are

$$u(1,z) = v(1,z) = 0 \quad T(1,z)) = \frac{8}{3} \quad p(r,0) = p_{\mathrm{IN}}$$
$$p(r,1) = p_{\mathrm{OUT}} \qquad u_r(0,z) = 0 \quad T_r(0,z) = 0$$

III. THE ISOTHERMAL APPROXIMATION

We first recall the main characteristics of the isothermal approximation obtained in Ref. [5] where the following set of the Navier-Stokes first-order solutions (labelled with the subscript 0) are for the temperature, the density gradient, the density change along the longitudinal axis, the flow rate, the pressure field, the longitudinal and the radial velocity compo-

nents, successively

$$T_0(r,z) = \frac{8}{3}$$
$$\frac{d\rho_0}{dz} = -\frac{2Q_0(3-\rho_0)^2}{3\rho_0(4-\rho_0)(\rho_0-1)^2}$$
$$z(\rho_0) = \frac{1}{Q_0}\left[\frac{\rho_0^3}{2} - \frac{18}{3-\rho_0} - 6\ln(3-\rho_0) + C_0\right]$$
$$Q_0 = \frac{\rho_{\mathrm{OUT}}^3 - \rho_{\mathrm{IN}}^3}{2} + \frac{18(\rho_{\mathrm{IN}}-\rho_{\mathrm{OUT}})}{(3-\rho_{\mathrm{OUT}})(3-\rho_{\mathrm{IN}})} + 6\ln\left[\frac{(3-\rho_{\mathrm{IN}})}{(3-\rho_{\mathrm{OUT}})}\right]$$
$$p_0(z) = \frac{3}{3-\rho_0}\left[(\rho_0-3)^3(\rho_0+3)+8\right] + C_1$$
$$u_0(r,z) = -\frac{4Q_0}{\rho_0}\left(1 - r^2\right)$$
$$v_0(r,z) = 0$$

$$(10)$$

The additional inlet constants C_0 and C_1 involved in the above solutions are

$$C_0 = -\frac{\rho_{\mathrm{IN}}^3}{2} + \frac{18}{3-\rho_{\mathrm{IN}}} - 6\ln(3-\rho_{\mathrm{IN}})$$
$$C_1 = \frac{3}{3-\rho_{\mathrm{IN}}}\left[(\rho_{\mathrm{IN}}-3)^3(\rho_{\mathrm{IN}}+3)+8\right]$$

In such an isothermal approximation, the near-critical nature of the fluid only plays through the equation of state and through the singular behavior of the isobaric expansion coefficient. Like in ideal-gas flows at the entry small scale of the capillary tube, the temperature is homogeneous (and equal to the critical temperature), the viscous friction is dominant and the basic dynamical structure is that of a Poiseuille flow along the longitudinal axis with zero-value of the radial velocity component. However, unlike ideal gas flows, the density gradient becomes infinite for the critical value of the density ($\rho_0 = 1$), which is reached in a so-called critical cross section defined by $z_c = z(\rho_0 = 1)$, (see left part of Fig. 2 where are reported non-dimensional density ρ_0 as a function of non-dimensional longitudinal z-coordinate for $r = 0$). In this critical cross section the pressure gradient keeps a finite value but the acceleration tends to infinity, which reveals the presence of a singular thermomechanical coupling mechanism crossing z_c. It is important to note that the fluid properties must be continuous throughout the flow field. It should be reminded that the total enthalpy of the fluid increases dramatically to keep its temperature constant in the strong fluid expansion at z_c. This is done by the heat transfer through the walls that was previously studied asymptotically in [5] from the second-order development of the variables, only using λ-model 1 for hydrogen case.

IV. THE HEAT TRANSFER

As for the above isothermal approximation, we first briefly report on the phenomenology of the heat transfer analysis performed in [5]. In this preliminary approach based on the λ-model 1 for the hydrogen case, the heat conduction diverges as $|\rho_0 - 1|^{-\frac{1}{2}}$, which is physically incorrect (see above), but allows obtaining a second-order asymptotic description from the equa-
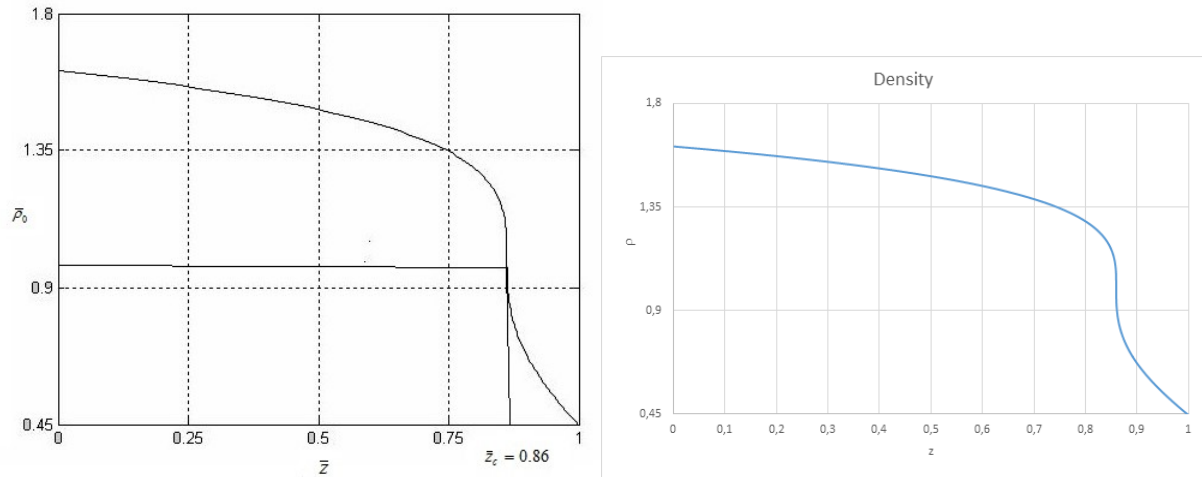
Figure 2: *left*: Rescaled density in the capillary tube, plotted as a function of the rescaled longitudinal z-coordinate, for hydrogen in the isothermal approximation and λ-model 1 for thermal conductivity. $p(z=0) = p_{\text{IN}} = 1.5$ and $p(z=1) = p_{\text{OUT}} = 0.8$. The density is continuous but its gradient is infinite at the critical cross section $z_c = z_0\,(\rho_0 = 1)$. *right*: Numerically computed density while keeping the temperature constant $T_0(r,z) = \frac{8}{3}$ (numerical isothermal approximation with similar condition to the left part case, see text).
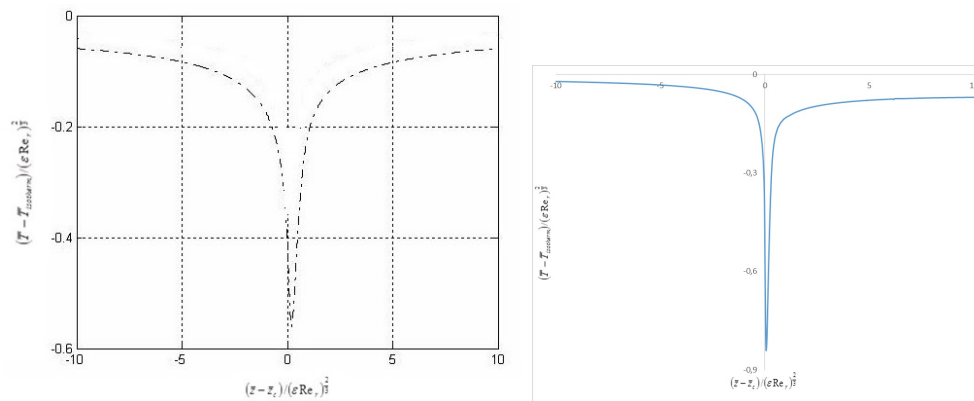

Figure 3: Rescaled temperature perturbation $\frac{T - \frac{8}{3}}{(\varepsilon \mathrm{Re}_R)^{\frac{2}{3}}}$ in the center of the capillary ($r = 0$) due to heat transfer in the narrow layer surrounding the critical cross section at z_c, plotted as a function of the rescaled variable $\frac{z - z_c}{(\varepsilon \mathrm{Re}_R)^{\frac{2}{3}}}$ for the non-isothermal approximation in hydrogen case with similar conditions to Fig. 2. *left*: As calculated from the second-order analytical solution in [5]. *right*: As computed from our numerical method.

tions that provides access to the basic thermal phenomena. Indeed, the introduction of such a simplified heat transfer in the asymptotic analysis highlights three regions. In the first region, that extends from the inlet section to the close vicinity of the critical cross section, the heat transfer is driven by a competition between the heat conduction and the heat sink due to the work of the pressure forces in the fluid flow expansion. The heat sink due to the expansion diverges such as $\sim \beta_p \sim (\rho_0 - 1)^{-2}$. The competition is in favor of the expansion so that the temperature perturbation goes to negative, infinite value, at z_c. The second region is a narrow layer perpendicular to the main stream, surrounding the critical cross section, driven by forced convection. In this layer the forced

convection brings heat from the upstream, hotter fluid and thus smooths out the singular temperature behavior. The singularity at z_c is replaced by a sharp drop in temperature over the narrow layer surrounding the critical cross section. The corresponding result is reported on the left part of Fig.3 that displays the rescaled temperature perturbation $\frac{T_0 - \frac{8}{3}}{(\varepsilon \mathrm{Re}_R)^{\frac{2}{3}}}$ as a function of the rescaled internal variable $\frac{z - z_c}{(\varepsilon \mathrm{Re}_R)^{\frac{2}{3}}}$ in such a narrow layer. We note that this dimensionless temperature drop and the corresponding dimensionless thickness of the layer scale as $\varepsilon\,(\mathrm{Re}_R)^{\frac{2}{3}}$. In the third region, that extends from the critical section to the outlet section, the fluid goes farther away from the critical point
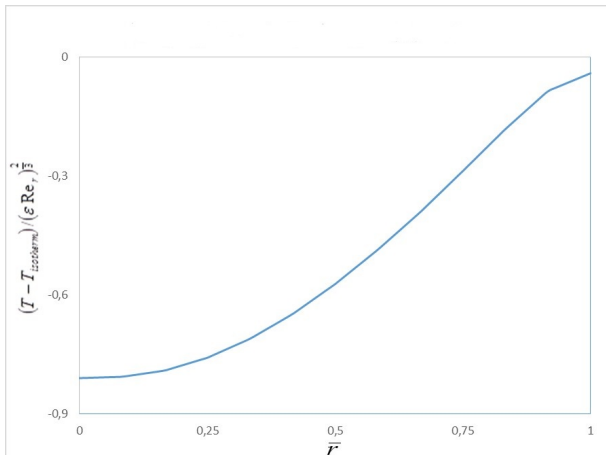
Figure 4: Numerically computed values of the rescaled temperature perturbation $\dfrac{T - \frac{8}{3}}{(\varepsilon \mathrm{Re}_R)^{\frac{2}{3}}}$ in the critical cross section at $z = z_c$, plotted as a function of the rescaled radius variable $\frac{r}{R}$ for the non-isothermal approximation in hydrogen case with similar conditions to Fig. 2. The apparent temperature difference at $\frac{r}{R} = 1$ is not physical but only due to the finite size mesh (see text).

since density keeps decreasing. Going away from the critical point makes the expansion process less and less effective to decrease the temperature, which increases again to ultimately reach the wall temperature in the outlet section. We note that the dynamic phenomena that occur in the critical cross section are not addressed in this preliminary work and we limit ourselves to the thermal effects only calculated numerically in the present work, first for λ-model 1 to validate the numerical method in hydrogen case, and second for λ-model 2 to estimate the order of magnitude of the amplitude of the non-isothermal effects for a more realistic heat conductivity for carbon dioxide case.

V. THE NUMERICAL METHOD

The numerical algorithm implemented in the PHOENICS software performs the discretization of the transport equations in a 2D, axisymmetric polar grid and uses a classical finite volume technique [9, 10]. This algorithm leads to a finite set of algebraic equations that are solved iteratively in a segregated manner. Such a task was accomplished using the BICGSTAB algebraic solver for temperature and velocities, and a preconditioned conjugate gradient for pressure. The density is estimated from the van der Waals equation of state in an iterative manner. The coupling between the momentum equation, the mass conservation equation, the energy equation and the equation of state is made using the SIMPLEST from the SIMPLE family algorithms. Moreover, the hybrid

scheme and or the CHARM second order scheme have been used to handle the discretization of the advection/convection term of the equations. The different steps of the resolution for each iteration increment (sweep) are summarized as follow:

1. Solve the density field and the thermodynamic pressure using a known temperature

2. Solve the momentum equations applying SIMPLEST algorithm

3. Solve the energy equation with the previously computed thermodynamic pressure at step 1

4. Repeat from step 1 for achieving convergence on a criteria calculated for each dependent flow variable. For this process, we need 4000 sweeps for the isothermal case to reach a steady state solution. Then using such isothermal case as initial, guess another 7000 sweeps to achieve steady state solution for non-isothermal case. The slowness of the convergence (due to the diverging properties around the critical point) to obtain the final temperature field $T(r, z)$ also impacts the resolution of the momentum and mass conservation equations. For the results presented in this paper, the number of points is 1000 in the axial direction and 12 in the radial direction.

VI. VALIDATION OF THE NUMERICAL CODE

A. The isothermal approximation for λ-model 1 (hydrogen)

In this section we consider λ-model 1 that has been used in the asymptotic analysis of Ref. [5], i.e., using $\lambda \sim (\rho_0 - 1)^{-\frac{1}{2}}$ along the critical isotherm. The temperature is first kept artificially to the critical temperature $T_0(r, z) = \frac{8}{3}$ during the calculation to compare with the isothermal analytical solution. The result shown on right part of Fig. 2 is in excellent agreement with the analytical one plotted on the left part.

B. Non isothermal numerical solution for λ-model 1 (hydrogen)

The excellent agreement between the second-order analytical results of Ref. [5] and our computed results for the temperature drop within the above-mentioned layer surrounding the critical cross section is shown on the left and right part of Fig.3 that displays the rescaled temperature perturbation as a function of the rescaled space variable. In addition, only considering the critical cross-section at $z = z_c$, the numerically computed evolution of the rescaled temperature perturbation as a function of the rescaled radius variable $\frac{r}{R}$ is shown in Fig. 4, which confirms the temperature relaxation to the thermostated temperature of
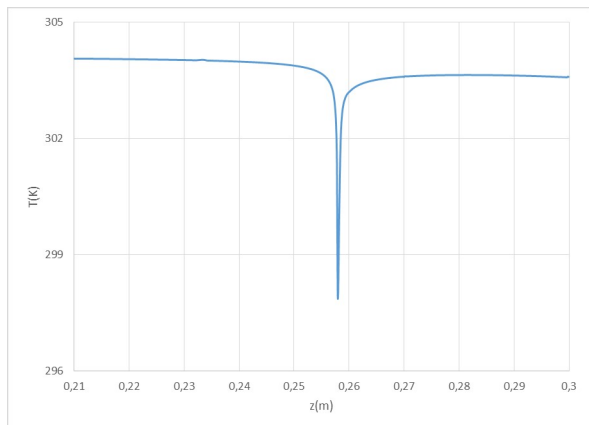
Figure 5: Numerically computed temperature of carbon dioxide (expressed in K) in the center of the capillary tube as a function of the z-abscissa (expressed in m) to show the expected dimensional temperature drop (here of $\sim -6\,\text{K}$) due to the thermal transfer effects, with the objective to perform an experiment control of the corresponding thermomechanical coupling mechanisms present in the narrow layer surrounding the critical cross section at $z_c \simeq 0.257\,\text{m}$.

the wall when $\frac{r}{R} \to 1$. We note that the apparent temperature difference at the wall limit $(r \simeq R)$ is not a physical result but only due to mesh finite size, while the numerically computed variables take the mean value at the volume center of the primary cell, which is in contact with the wall boundary. Although further refinements in the mesh size for the stability of the solution are still pending, we can proceed to the similar numerical calculation for the carbon dioxide case that accounts for a more realistic behavior of the thermal conductivity.

C. Non isothermal numerical solution for real heat conductivity (λ-model 2, carbon dioxide)

The calculations are performed for CO_2, considering Eq. 8 with the fluid parameters given in Table II or in the text, *i.e.*, using $\Delta\lambda \sim (\rho_0 - 1)^{-1}$ along the critical isotherm. μ_{IG} and λ_{IG} are calculated only from the term corresponding to the zero-density limit contribution to μ and λ, respectively, at $T = T_c$ (see [8]). Moreover, we note the relative reduction of the inlet pressure to $p_{\text{IN}} = 1.05\,p_c$ and the outlet discharge

pressure to $p_{\text{OUT}} = 0.95\,p_c$, from comparison to the previous hydrogen case. The computed temperature within the longitudinal axis of the capillary tube is given in Fig. 5. We note the non-symmetry of the temperature profile that comes from the regular part $\overline{\lambda}(T, \rho)$ of the thermal conductivity, which exhibits a monotonic increase with increasing density (along the critical isotherm). This noticeable realistic feature (which is not possible to reveal by using the symmetrical simplified λ-model 1) provides confidence in using our numerical method for designing the future experiment that will be performed to validate the robustness of this thermomechanical coupling mechanism in confined transcritical fluid flows in capillaries.

VII. CONCLUSIVE REMARKS

Using a realistic description of the singular behavior of the thermal conductivity close to the critical point of carbon dioxide, we have numerically confirmed the main features of the thermomechanical coupling mechanisms of a van der Waals fluid flow passing through the critical state on its way along a capillary tube. Particular attention was focused on the effect of thermal transfers through the wall as previously observed from an analytical asymptotic analysis [5]. Our results show a significant decreasing amplitude of the carbon dioxide temperature profile crossing the critical cross section. These results, related to a real fluid easily used in confined channels [11, 12], open a possible alternative route for the experimental validation of these modelling approaches. Indeed, a local temperature drop below the critical temperature can then drive a phase separation process in the capillary flow, provided the local density reaches the unstable two-phase region under the liquid-gas coexistence curve. The numerical investigations of the density behavior near the critical cross section are in progress to check this confined two-phase conjecture.

[1] H.E. Stanley H. E. , Introduction to phase transition and critical phenomena, *Clarendon Press, Oxford Science Publication* (1971).

[2] Wilson K.G. and Fisher M.E., Critical exponents in 3.99 dimension, Phys. Rev. Lett., 28,240-243 (1972).

[3] Gitterman, M. Hydrodynamics of near critical fluids near a critical point, Rev. Mod. Phys., 50, 85 (1978).

[4] Zappoli, B., Beysens D., Garrabos, Y., Heat Transfers and Related Effects in Supercritical Fluids, Springer, http://link.springer.com/book/10.1007%2F978-94-017-9187-8.

[5] Khelalfa R., Laugerais P.-O., Durastanti J.-F., and Darrozès J.-S., Study of fluid flow passing through the vicinity of the critical point, *J. Thermophysics*

and Heat Transfer, 28, 303-312 (2014).

[6] Zappoli B., Bailly D., Garrabos,Y., Le Neindre B., Guenoun P. and Beysens D., Phys. Rev. A Rap. com. 41, 2264 (1990).

[7] Gitterman, M and Steinberg, V. A., Criteria of occurence of free convection in a compressible viscous fluid, J. Appl. Math., 34, 305 (1970).

[8] J.V. Sengers, R.S. Basu, J.M.H Levelt Sengers, Representative Equations for the Thermodynamic and Transport Properties of Fluids Near the Gas-Liquid Critical Point, NASA Contractor Rep. 3424 (1981).

[9] S.V. Patankar, Numerical heat transfer and fluid flow,

Hemisphere Publishing Corporation (1980).

[10] J. Ouazzani and Y. Garrabos, Proc. AsME Heat Trans.Conf., 2013, 3-HT2013-17732, Asme, N.Y. (2013).

[11] N. Liu, C. Aymonier, C. Lecoutre, Y. Garrabos, S. Marre, Microfluidic approach for studying CO_2 solubility in water and brine using Raman confocal spectroscopy, Chem. Phys. Lett., 551, 139 (2012).

[12] M. Abolhasani, A. Günther, and E. Kumacheva, Microfluidic Studies of Carbon Dioxide, Angew. Chem. Int. Ed., 53, 7992 (1014).

AERODYNAMICALLY EFFICIENT BUS DESIGNS INSPIRED BY BELUGA WHALES

Kırmacı Arabacı S. and Pakdemirli M.*

*Author for correspondence

Department of Mechanical Engineering,

Celal Bayar University,

Manisa,

Turkey,

E-mail: mpak@cbu.edu.tr

ABSTRACT

In this work, flow analysis, drag forces and drag coefficients of various bus models are investigated. Reduced drag forces result in lower fuel consumptions. The geometrical shape of the bus is very important for efficient streamlining and reduced drag. For a given volumetric inner space, the goal would then be to search for optimum shapes. For those shapes, inspiration is taken from nature. Due to its highly efficient hydrodynamics body, beluga whale shape is taken as an example and similar forms are designed for buses. The body is drawn using UNIGRAPHICS program. The drawings are then inserted into ANSYS CFD program for meshing. Drag forces and drag coefficients corresponding to the various designs are determined using Fluent (solver) and CFX (result) program. Substantial reduction in drag coefficients is possible for these new geometries which are inspired from whales.

INTRODUCTION

Biomimetic is a branch of science where technological improvements are achieved by mimicking designs from nature. Structures and design of creatures are sources of inspiration for scientists. A further jump in the current advanced level of technology can be possible by taking examples from nature and applying the concepts for solving our problems [1].

Imitating forms from nature leaded to improvements in design concepts recently. Structure of humpback whale fins were investigated and the bumps known as tubercules could reduce drag and increase lift. Similar bumps could lead to more-stable airplane designs, submarines with greater agility, and turbine blades that can capture more energy from the wind and water [2]. A robot fish were designed and fabricated that mimics motion of a fish with oscillation of its tail fin [3].

Nowadays, the scientists work hard to improve the performance of vehicle by modifying the shape and weight of the vehicle. A recent research about fuel reduction for vehicles showed that aerodynamic improvement is one of the most important technologies when it comes to fuel saving [4]. A new concept car named bionic car has been designed by Mercedes-Benz engineers mimicking the form of a boxfish. The drag coefficient of the car reached a very low value of 0.19 [5, 6]. Usually, in such car models the drag coefficients are within the range of 0.30-0.35.

By modifying the truck geometry, solving the Navier-Stokes equation with k-ε turbulence model, it is shown that estimated fuel savings is nearly 35% [7]. Mohamed *et al.* [8] studied the possibility of drag reduction of buses and found that reduction in aerodynamic drag up to 14% can be reached, which corresponds to 8.4% reduction in fuel consumption by slight modification of the outer shape. In another bus model, a comparison with the worst design is made and the drag coefficient is reduced from 0.8782 to 0.3872 by using a curved surface in front. [9]. Airbus designed a cargo plane A300-600ST which was inspired by the form of beluga whales and commonly known as Airbus Beluga [10]. Due to their high volumetric shape and perfect streamlined bodies, beluga whales are taken as examples to construct one of the worlds' greatest aeroplanes.

In this study, the perfect shapes of beluga whales are mimicked to reduce drag forces and coefficients of buses. Different new models were constructed all inspired by the beluga geometry. Solid models of the new buses are drawn using Unigaphics program. The models are placed in a control volume in Ansys CFD program. Drag forces and drag coefficients are calculated for these new designs.

NOMENCLATURE

A	[m^2]	Frontal cross-sectional area of object
C_d	[-]	Drag coefficient based on A
C_f	[-]	Skin friction
D	[m]	Characteristic diameter
F_d	[N]	Drag force (total)
h	[m]	Height
L	[m]	Length
N	[m]	Width
P	[Pa]	Pressure
V	[m/s]	Velocity of object
y	[m]	First boundary layer thickness in CFX mesh

Special characters

ρ	[kg/m^3]	Flow density
μ	[kg/ms]	Dynamic viscosity
U^*	[m/s]	Friction velocity
τ_ω	[Pa]	Wall shear stress

Subscripts

|	
CFD	Computational fluid dynamics
Re	Reynold number

| 2D | Two dimensional |
| 3D | Three dimensional |

MATERIALS

New designs of buses are presented to reduce drag and hence fuel consumption. Beluga whales are taken in the development of the solid models. The whales are chosen because they have a high volumetric space similar to buses and an excellent streamlined body with low drag values. Belugas grow up to 5.5 m in length and weighs up to 1600 kg. It has a swimming speed of 3-9 km/h, although they can maintain speeds as high as 22 km/h lasting up to 15 min [11].

In this study, drag forces and drag coefficients of the new designs are contrasted with the commercial Neoplan Skyliner bus model which has one of the lowest drag coefficient value. The model and the dimensions are given in Figure 1 [12]. The company MAN Truck & Bus AG, announces the drag coefficient of the bus as 0.41. This is one of the lowest values among different commercial bus models.

Solid model of the Skyliner is drawn using Unigraphics program as shown in Figure 2. The total length of the bus is 14 m, the width is 2.55 m, and the height is 4 m.
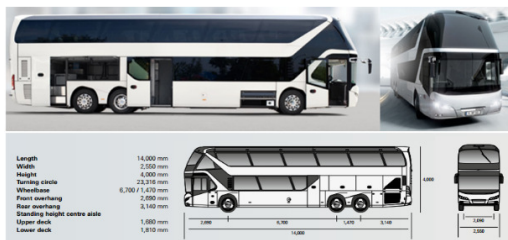

Figure 1 Neoplan Skyliner Bus

Figure 2 Neoplan Skyliner model drawn by Unigraphics

The solid model of the beluga whale is formed using the same drawing program. First, splines of the solid model are drawn in 2D using Autocad program. The 3D shape is then formed by Unigraphics program as shown in Figure 3. The dimensions of beluga whales are taken as 1.066 m height, 0.944 m width and 5.493 m length. The volume of the solid whale is 2.33 m^3.
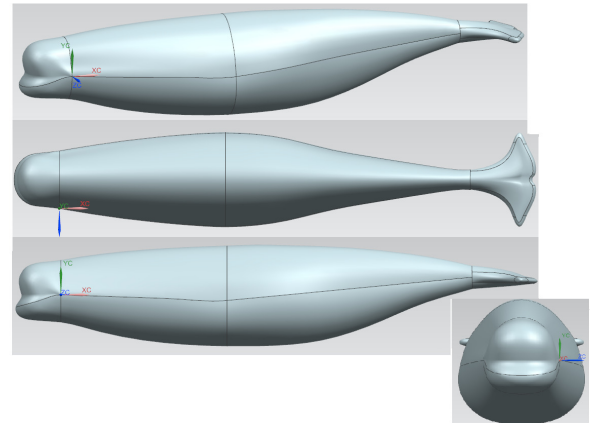
Figure 3 Beluga whale 3D model drawn by Unigraphics

Six different variants of the beluga bus models are developed and specific names are assigned. The names are Beluga 1.1, Beluga 1.2, Beluga 1.3, Beluga 2.1, Beluga 2.2, and Beluga 2.3. The shapes of each model are given in Figure 4. The first number refers to the shape of the frontal part of the bus and the second number refers to the rest of the body including the middle and rear part of the bus. In accordance, Beluga 1.x models all have the same frontal shape, whereas Beluga x.1 all have the same body shape.

The bus with original volume is named as Skyliner.N and the bus with a slightly reduced volume which has equivalent volume with the new designs is called Skyliner.V.

Slight reductions in width and height is observed in Beluga 1.1 model when viewed from above and sides. The frontal cross sectional area is designed to be wider than the rear cross sectional area.

In Beluga 1.2 model, the design of frontal part is same with that of 1.1 model but the body differs. From front to rear, the height and width increase slightly first and then decrease towards the rear part. Excluding the frontal design, Beluga 1.3 has an identical body shape with the Skyliner body.

In Beluga 2.x models, the frontal design has been changed and the frontal shape looks sharper. Beluga 2.1 and 1.1 have the same body shapes except the frontal design and so on.

The original Neoplan Skyliner which is named as Skyliner N has a volume of 122.8 m^3. Instead of generating Beluga models with 122.8 m^3 volumetric space which will not be suitable in dimensions according to 128th article of Highway Regulations, a reduced model of 100 m^3 volumetric space is selected for both the new designs and Skyliner models. The corresponding Skyliner model with 100 m^3 is called Skyliner.V.

Beluga 1.1

Beluga 1.2

Beluga 1.3

Beluga 2.1

Beluga 2.2

Beluga 2.3

Figure 4 Beluga Buses

NUMERICAL METHODS

The models are replaced in a control volume with dimensions 12 m, 22.5 m and 98 m in Ansys Workbench program. The model is placed in the control volume with twice the bus length from the inlet, four times the bus length from the outlet and 8 times the bus width from sides. Blockage ratio is defined to be the ratio of cross-sectional area of the prototype to the cross-sectional area of the control volume. For reliable results this ratio is kept under 7.5% in this study.

Mesh Converter

The model is replaced within two rectangular prism shaped boxes as shown in Figure 5. A finer mesh size is taken in the inner box. As an indication of the quality of the meshing, maximum skewness is kept under 0.95 in Ansys mesh.
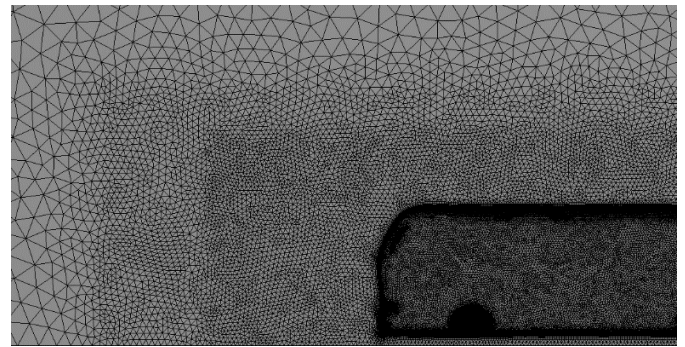

Figure 5 Meshing of Skyliner.N Model

Six different number of total meshes are used to test the mesh-independency as given in Figure 6. The fourth test (7,671,773 number of meshes) is observed to be ideal for convergence of the results. Max. skewness ratio is found to be 0.837.
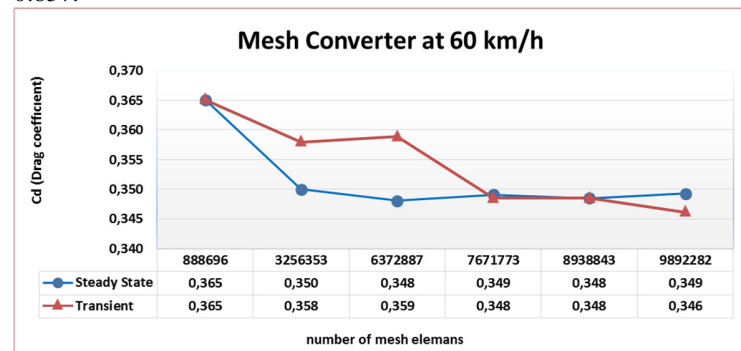

Figure 6 Mesh converter at 60 km/h

Boundary Conditions

The boundary conditions of the domain are: 60 km/h velocity at the inlet surface, zero pressure-gradient at the outlet, no slip condition at the road and bus, free slip condition at the sides. The road is taken to be both stationary and moving. The surfaces of the control volume are defined to have no shear stress whereas the surface of the bus is defined to have no slip condition.

The temperature, density of air and dynamic viscosity values used in the analysis are taken as 20ºC, 1.205 kg/m^3 and 1.8206 x 10^{-5} kg/ms, respectively.

The drag force is

$$F_d = 0.5\rho C_d A U^2 \tag{1}$$

where ρ is the fluid density, C_d is the drag coefficient, A is the cross sectional area vertical to the air flow direction of the bus and V is the fluid velocity. The cross-sectional areas of Skyliner N., Skyliner V., Beluga 1.1, Beluga 1.2, Beluga 1.3, Beluga 2.1, Beluga 2.2 and Beluga 2.3 are taken as 4.692 m^2, 4.089 m^2, 4.309 m^2, 4.208 m^2, 4.145 m^2, 4.371 m^2, 4.274 m^2 and 4.202 m^2 respectively.

The Reynolds number is

$$Re = \frac{\rho V^2 L}{\mu} \tag{2}$$

where L is the length of the model and μ is the dynamic viscosity. In the flow analysis, another important issue is the boundary layer thickness. During the CFD pre-processing stage, we need to know a suitable size for the first layer of grid cells (inflation layer) so that y^+ is in the desired range. The actual low-field will not be known until we have computed the solution (and indeed it is sometimes unavoidable to have to go back and remesh your model on account of the computed y^+ values). To reduce the risk of needing to remesh, we may want to try and predict the cell size by performing a hand calculation at the start.

Boundary layer analysis should be included in the analysis. The parameters are

$$C_f = 0.058 \, Re^{-0.2} \tag{3}$$

$$\tau_w = 0.5 \rho C_f V^2 \tag{4}$$

$$U^* = \sqrt{\frac{\tau_w}{\rho}} \tag{5}$$

$$y = \frac{y^+ \mu}{U^* \rho} \tag{6}$$

where C_f is the skin friction, τ_ω is the wall shear stress, U^* is the friction velocity. In the aerodynamic analysis, the reference displacement should be $y^+ \leq 1$ [13]. In this paper, $y^+=1$ is used and the turbulence model is selected as k-ω SST model which is recommended for external flow. First boundary layer thickness y is found by taking $y^+=1$ and shown in Figure 7.
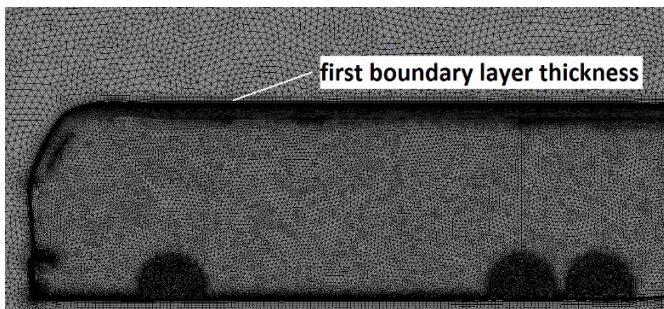

Figure 7 Boundary layer thickness

RESULTS

The CFD results of the Neoplan Skyliner and various beluga models are given in this section. The first boundary layer thicknesses, Reynolds numbers, drag coefficients and total drag forces are given in Table 1 for inlet fluid velocities of 60 km/h, $y^+=1$ and k-ω SST turbulence model.

Table 1 Drag forces and coefficients of the models

Models	y (m)	Re	Stationary Road		Moving Road	
			C_d	F_d(N)	C_d	F_d(N)
Skyliner .V	4.02E-05	1.44E+07	0.382	261.6	0.401	274.1
Beluga 1.1	4.04E-05	1.50E+07	0.327	235.5	0.317	228.1
Beluga 1.2	4.03E-05	1.47E+07	0.277	195.1	0.280	196.9
Beluga 1.3	4.03E-05	1.46E+07	0.321	222.7	0.320	222.1
Beluga 2.1	4.04E-05	1.52E+07	0.335	244.9	0.324	236.6
Beluga 2.2	4.03E-05	1.48E+07	0.289	206.8	0.290	207.6
Beluga 2.3	4.03E-05	1.47E+07	0.328	230.5	0.324	228.0

Skyliner N. is the original model and the obtained values can be compared with the one provided by MAN Truck & Bus AG. The company provides a value of 0.41. For stationary road, our calculated value is 0.349 and for moving road it is 0.361. Result of moving road seems to be closer to the given value. The reasons for discrepancy might be the absence of rearview mirrors and some other minor details as well as the perfect smoothness of the surfaces in our model which decreases the drag. Drag force of Skyliner.N is 273.9 N in stationary road, 283.2 N in moving road.

Drag coefficients and total drag forces of buses of equal volumes are shown in Figures 8 and Figure 9.
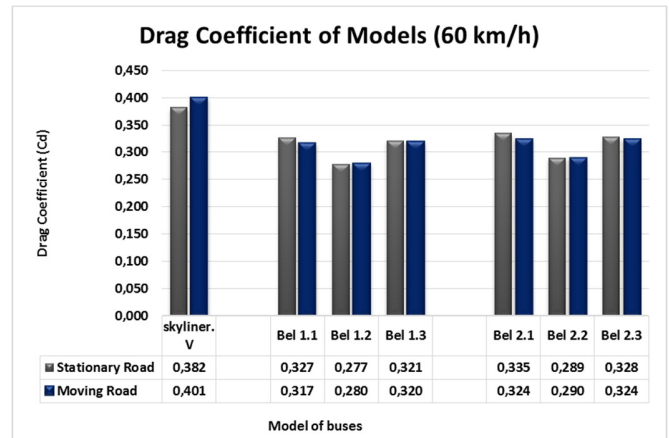

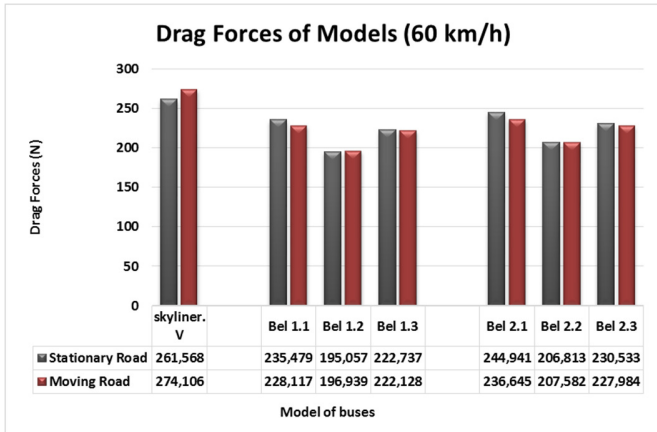**Figure 8** Drag Coefficient of models at 60 km/h

Figure 9 Drag Forces of models at 60 km/h

Reduction in drag coefficients and forces are achieved in all beluga models. One may conclude that the aerodynamic design of buses can be improved by mimicking beluga whales. The perfect streamlined shape of belugas are the reason of such reduction. Among the six variants of the beluga models, the best is Beluga 1.2 with the lowest drag coefficient of 0.277 in stationary road and 0.280 in moving road. Drag coefficients of the Skyliner.V is highest compared to the new designs with 0.382 for stationary road and 0.401 for moving road.

The static pressure contours of the three buses are given in Figure 10. These contours reveal the pressure variations and their areas of application.
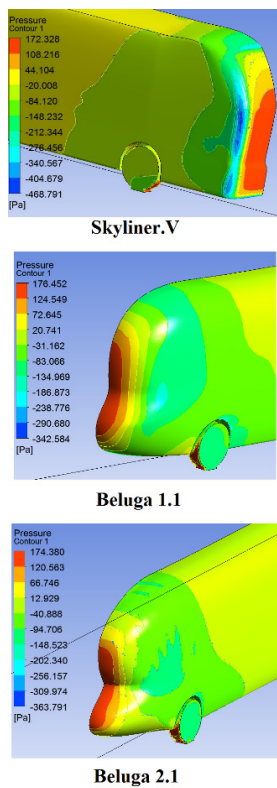

Figure 10 Static pressure contours of three models

The max. Pressure of Skyliner.N is 172.1 Pa in stationary road, 183.8 Pa in moving road. The maximum static pressures of the models are given Table 2.

Table 2 Max. Pressures of models

Models	Max.Pressures of models in Stationary Road (Pa)	Max.Pressures of models in Moving Road (Pa)
Skyliner.V	172.3	170.0
Beluga 1.1	172.2	178.1
Beluga 1.2	174.2	183.3
Beluga 1.3	181.1	180.8
Beluga 2.1	174.4	180.6
Beluga 2.2	171.6	174.9
Beluga 2.3	171.9	174.3

The highest static pressure is observed in Beluga 1.3 which is 181.1 Pa, and the lowest is in Beluga 2.2 which is 171.6 Pa. The maximum pressure area is widest in Skyliner V which does not have a perfect streamlined shape and in beluga models, the maximum pressure areas are reduced substantially.

Streamlines for the models are shown in Figure 11. Eddy formation is observed at the rear of the models.
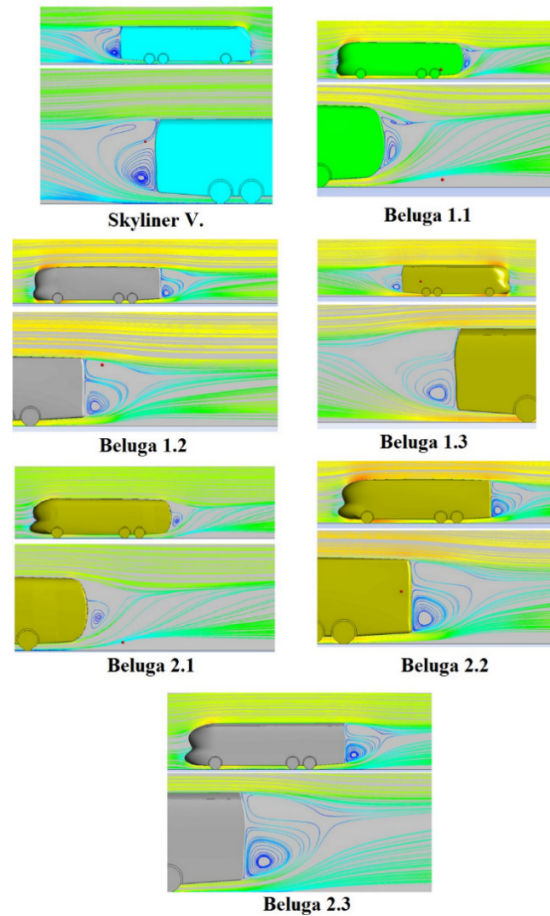

Figure 11 Streamlines and eddies of models

The eddy formation at the rear is associated with the body design (mostly middle and rear parts). It is observed that Beluga x.1 models have smaller eddies compared to others. Beluga x.2 and x.3 models as well as the Skyliner models lead to larger eddies.

CONCLUSION

In this study, new bus designs are proposed to increase the aerodynamic efficiency. Inspired by the beluga whales, six different variants of the beluga bus designs are contrasted with the commercial Skyliner model which has one of the lowest drag coefficients among the bus models in use. It is shown that substantial reductions can be achieved in mimicking the form of a beluga whale. The flow analysis is conducted for 60 km/h (16.66 m/s) inlet velocities. It is shown that the drag coefficients can be reduced to lower values of 0.28 compared to some common designs of drag values as high as 0.40. Those models have 6 wheels and not including rearview mirror.

While reductions are achieved in all six variants of the models, the best is Beluga 1.2 model with a drag coefficient reduction of 27.4% in stationary road, 30.17% in moving road.

REFERENCES

[1] Benyus JM., Biomimicry: Innovation inspired by nature, *New York: William Morrow and Company, Inc*., 1997.

[2]http://www.technologyreview.com/news/409710/whale-inspired-wind-turbines/ (Access date: 16.04.2015)

[3] Mohammad Shahi D., Yousefi-Koma A., Bahmanyar S., Maleki H., Design, fabrication and hydrodynamic analysis of a biomimetic robot fish, *10th Wseas Int. Conf. On Automatic Control, Modelling & Simulation (Acmos'08),* Istanbul, Turkey, May 27-30, 2008.

[5] Neurohr R., Dragomirescu C., Bionics in engineering - Defining new goals in engineering education at Politehnica University of Bucharest, *International Conference on Engineering Education, ICEE,* Coimbra, Portugal, September 3 – 7, 2007.

[6] Ellenrieder G., Mercedes-Benz bionic car, Fachtagung, *Bionik im Automobil Ulm*, Germany, 6&7 Dezember 2005.

[4] Håkansson C., Lenngren M.J., CFD Analysis of aerodynamic trailer devices for drag reduction of heavy duty trucks, *Master's Thesis in the Master's programme Automotive Engineering*, Chalmers University of Technology, Göteborg, Sweden, 2010.

[7] Roy S., and Srinivasan P., External Flow Analysis of a Truck for Drag Reduction, *International Truck and Bus Meeting & Exposition,* Paper: 2000-01-3500, 2000.

[8] Mohamed E.A., Radhwi M. N., Abdel Gawad A.F., Computational investigation of aerodynamic characteristics and drag reduction of a bus model, *American Journal of Aerospace Engineering*, vol.2, No.1, pp. 64-73, 2015.

[9] Bhave A. and Taherian H., *Aerodynamics of Intercity Bus and its Impact on CO_2 Reduction*s, Proceedings of the Fourteenth Annual Early Career Technical Conference, The University of Alabama, Birmingham ECTC 2014, November 1 – 2, 2014 - Birmingham, Alabama USA

[10] Airbus- http://www.airbus.com/aircraftfamilies/freighter/beluga (Access date: 16.04.2015)

[11] Nowak, Ronald M., *Walker's Mammals of the World 2* (5 ed.), Baltimore: The Johns Hopkins University Press, ISBN 0-8018-5789-9,1991.

[12] http://www.neoplan-bus.com/cms/de/skyliner/index.html (Access date: 16.04.2015)

[13] Frank T., Gerlicher B., Abanto J., "*Drivaer-Aerodynamic Investigations, USA for a New Realistic Generic Car Model using ANSYS CFD*, ANSYS Inc Tutorial, Germany, September 2013.